

The Vertical Structure of the F Ring of Saturn from Ring-Plane Crossings

Britt R. Scharringhausen*

Department of Physics and Astronomy, Beloit College, Beloit, WI, 53511

Philip D. Nicholson

Department of Astronomy, Cornell University, Ithaca, NY, 14853

Abstract

We present a photometric model of the rings of Saturn which includes the main rings and an F ring, inclined to the main rings, with a Gaussian vertical profile of optical depth. This model reproduces the asymmetry in brightness between the east and west ansae of the rings of Saturn that was observed by the Hubble Space Telescope (HST) within a few hours after the Earth ring-plane crossing (RPX) of 10 August 1995. The model shows that during this observation the inclined F ring unevenly blocked the east and west ansae of the main rings. The brightness asymmetry produced by the model is highly sensitive to the vertical thickness and radial optical depth of the F ring. The F-ring model that best matches the observations has a vertical full width at half maximum of 13 ± 7 km and an equivalent depth of 10 ± 4 km. The model also reproduces the shape of the HST profiles of ring brightness vs. distance from Saturn, both before and after the time of ring-plane crossing. Smaller asymmetries observed before the RPX, when the Earth was on the dark side of the rings, cannot be explained by blocking of the main rings by the F ring or vice versa and are probably instead due to the intrinsic longitudinal variation exhibited by the F ring.

1. Introduction

With a semimajor axis of 140,200 km (Bosh et al., 2002), the F ring of Saturn lies ~ 3500 km outside the A ring. The narrow F ring is largely diffuse and dusty, composed of particles $\sim 0.5\mu\text{m}$ in size, with a highly variable optical depth that is generally < 1 . It may have a narrow core of greater optical depth, composed of macroscopic particles (Showalter et al., 1992). Because the F ring lies just outside the main rings and is only weakly backscattering, it is usually not observable from Earth. An exception occurs during a ring-plane crossing (RPX), when the small ring-opening angle drastically reduces the brightness of the main rings to levels comparable to, or less than, the brightness of the F ring.

The Sun crosses Saturn's ring plane during the equinoxes of Saturn, approximately every 15 years. As Saturn's ring plane sweeps through the inner Solar System, Earth's orbital motion carries it from one side of Saturn's ring plane to the other. During each ring-plane-crossing season, which takes less than 12 months, there is one solar RPX. In about half of RPX seasons, the Earth crosses the ring plane three times, with one Earth ring-plane crossing occurring near opposition; the last such event occurred on 10 August 1995.

*Corresponding author:

Britt Scharringhausen
Beloit College
Beloit, WI 53511
Email: scharr@beloit.edu
Phone: (608) 363-2648
Fax: (608) 363-2052

Email addresses: scharr@beloit.edu (Britt R. Scharringhausen), nicholso@astro.cornell.edu (Philip D. Nicholson)

In the other half there is only one Earth ring-plane crossing which occurs near solar conjunction and is thus generally not observable from Earth (as was the case in the RPX of 2009).

An Earth RPX gives us an excellent opportunity to probe the F ring's properties. During an RPX, the observed brightness of the main rings is greatly reduced but because the F ring is optically thin, its brightness is unaffected. When the Earth is on the dark side of the main rings near RPX, the F ring dominates the overall brightness of the rings. Even when Earth is on the lit side of the rings, the brightness of the F ring is comparable to the brightness of the main rings when the ring-opening angles to Earth and the Sun are small. Due to its vertical thickness, the F ring also can partially obscure the main rings and so can block some of their reflected sunlight. This means that the overall brightness of the rings during an Earth ring-plane crossing cannot be understood without understanding the role of the F ring.

Early observers were stymied when attempting to measure the thickness of Saturn's rings during previous Earth ring-plane crossings, finding thicknesses much greater than measurements of the main ring thickness derived from theoretical estimates and Voyager observations. An asymmetry in brightness between the east and west ansae near the Earth ring-plane crossing of 10 August 1995 also could not be explained using the known properties of the main rings. In this paper we will show that the F ring provides the solution to both of these puzzles.

1.1. Early estimates of ring thickness

Historically, an Earth RPX has been seen as an opportunity to measure the vertical thickness of the rings as they are seen edge-on. The vertical thickness of the rings is too small to be resolved, even by spacecraft (Goldreich and Tremaine, 1978; Esposito et al., 1984; Zebker et al., 1985; Salo and Karjalainen, 2003). The projected height of the rings on the sky is small enough that from Earth the rings are vertically unresolved for weeks before and after the RPX. Prior to Voyager, the residual ring brightness at the moment of the RPX was generally assumed to be due to light reflected from the outer edge of the A ring and possibly the edge of the B ring seen through the Cassini Division (Brahic and Sicardy, 1981).

The brightness of the rings, expressed as an equivalent photometric thickness with units of length, was traditionally interpreted using radiative transfer theory to estimate the physical thickness of the rings. Based on various observations of the 12–13 June 1966 RPX, the photometric thickness of the rings was found to be 0.57 km (Bobrov, 1972), $0.8^{+2.3}_{-0.8}$ km (Lumme and Irvine, 1979), 1.3 ± 0.3 km (Fountain and Larson, 1978), and 2.4 ± 1.3 km (Dollfus, 1979). These measurements were taken from photographic plates and the ring's edge-on reflectance was assumed to be similar to the reflectance of Saturn. By modeling the rings as a plane-parallel scattering layer of finite thickness, Sicardy et al. (1982) found a thickness of $1.1^{+0.9}_{-0.5}$ km using observations of the RPX of 12 March 1980.

These photometric ring thicknesses are significantly larger than measurements of the main ring thickness obtained by interpreting various types of spacecraft observations.

1.2. Voyager observations of ring thickness

An occultation of the star δ Scorpii by the rings was observed using the Voyager 2 Photopolarimeter Subsystem (PPS). By measuring the rate of change of the transmitted flux of the occulted star as it crossed several sharp transitions from opaque to transparent regions of the main rings, an upper limit of 200 m was placed on the thickness of the main rings (Lane et al., 1982). Measurements of the forward-scattering of microwaves transmitted through the rings from Voyager 1 indicated a thickness of 10 m in the C ring and 20–50 m in the A ring (Zebker and Tyler, 1984) although the results are somewhat model-dependent.

Based on the damping distance of density and bending waves in the rings, Esposito et al. (1984) argued for a main-ring thickness of 30–35 m. Goldreich and Tremaine (1978) modeled the ring particles as inelastically colliding spheres and concluded that, if the rings have come to an equilibrium between viscous dissipation and stirring by collisions, their vertical thickness is likely to be less than 10 m. If less elastic collisions are assumed, the model implies that the rings will collapse to a monolayer.

Salo and Karjalainen (2003) combined a sophisticated dynamical model of the rings with a Monte Carlo photometric model. The B ring's increased brightness at opposition (the opposition effect) and increasing brightness at larger opening angles (the tilt effect) were best reproduced by a model with a distribution of

particle sizes from 10 cm to 5 m, although this lower limit is slightly too high to be consistent with the particle size distribution derived from the Voyager radio occultation experiment (Zebker et al., 1985). In this model, the larger particles settled into a near-monolayer, though the smaller particles had a vertical distribution of a few tens of meters.

While occultation measurements and dynamical models of the rings vary in their estimates of the thickness of the rings, none of these models provides a ring thick enough to account for the residual brightness of the rings during an Earth RPX, although Lissauer et al. (1984) found that the Mimas 5:3 bending wave in the A ring has a vertical amplitude of 500 m, which may account for part of the observed edge-on brightness.

1.3. The 1995 ring-plane crossings

Assuming a geometric albedo of 1 for the rings, Bosh et al. (1997) estimated an equivalent thickness of 1.4 ± 0.1 km from Hubble Space Telescope (HST) images taken during the Earth ring-plane crossing of 22 May 1995, while Nicholson et al. (1996) found a vertically-integrated reflectance of 1.22 ± 0.17 km for the east ansa and 1.53 ± 0.09 km for the west ansa. (These figures do not suffer from the calibration problem to be discussed in Sec. 2.2.) Both of these thicknesses are similar to earlier ground-based photometric thicknesses.

Profiles of brightness as a function of radius from the set of HST images spanning the August 1995 Earth RPX showed two surprising features. In images of the dark side of the rings, when one would expect very little light from the main rings, the profile of ring brightness as a function of distance from the center of Saturn (see Fig. 1) is fairly uniform out to the semimajor axis of the F ring, where it drops rapidly, suggesting that the primary contribution to the ring brightness in this geometry comes from the F ring (rather than the Mimas bending wave at $\sim 133,000$ km). A more surprising discovery was that the radially-averaged brightness of the rings was greater on the west ansa than the east ansa, with this asymmetry reversing ~ 3 hours after the ring-plane crossing. (Nicholson et al., 1996)

In HST observations of the dark side of the rings at an Earth ring-opening angle of $B_e = 2.67^\circ$ obtained during the November 1995 solar RPX, the F ring is prominent at the edge of the main rings, but disappears $\sim 35^\circ$ to the rear of the east ansa, suggesting that the F ring is inclined and that it was being shadowed by the main rings (Olkin and Bosh, 1996; Nicholson et al., 1996).

We exploit this asymmetry to find the equivalent depth and vertical extent of the F ring.

2. HST observations of the 10 Aug 1995 ring-plane crossing

HST observed the Earth ring-plane crossing on 10 August 1995. The $0.89 \mu\text{m}$ methane filter (FQCH4N) was used to reduce scattered light from Saturn without suppressing the brightness of the rings. HST’s orbit around the Earth has a 96-minute period so that “visits,” or observing opportunities, were ~ 20 – 40 minutes in duration. We group the images into seven visits which we label with the round times 14:00, 15:30, 18:30, 20:00, 22:00, 23:30, and 25:00. All times are given in UT. The last time is actually 1:00 UT on 11 August 1995. From 14–20 UT, the Earth was on the dark side of the main rings, and from 22–25 UT the Earth was on the sunlit side.

In each visit, images were taken with the Planetary Camera (PC) and the Wide-Field Camera (WF3), which were the first and third chips, respectively, of the Wide-Field Planetary Camera 2 (WFPC2). Table 1 gives the approximate times of each of these HST visits and the ring-opening angles at these times. The pixels in the WF3 images have a size of 634.2 km at Saturn, and the images include both ring ansae. PC images, at 290.0 km/pixel, have a smaller field of view, and contain only one ansa (the east ansa until 23:00, and the west ansa thereafter). For further details of the observation sequence, image numbering, etc., the reader is referred to McGhee et al. (2001).

2.1. HST profiles

During the HST observations, the projected “height” of the main ring ($2R_A \sin B_e$, where R_A is the outer radius of the A ring) was $\lesssim 40$ km, much less than the image resolution of $0.1 \text{ arcsec} \approx 650$ km, so the rings are unresolved in the vertical dimension and remain so for $|B_e| < 0.14^\circ$, approximately 4 days before and after the August 1995 RPX. The ring-opening angles for each visit are given in Table 1. Profiles were

Table 1: Earth and Sun ring-opening angles (B_e and B_s , respectively) for HST observations, interpolated from an ephemeris provided by the Planetary Data System’s Rings Node.

UT Date and Time		$B_e(^{\circ})$	$B_s(^{\circ})$
1995 Aug. 10	14:00	-0.0078	1.498
1995 Aug. 10	15:30	-0.0061	1.497
1995 Aug. 10	18:30	-0.0026	1.496
1995 Aug. 10	20:00	-0.0008	1.495
1995 Aug. 10	22:00	0.0015	1.493
1995 Aug. 10	23:30	0.0031	1.492
1995 Aug. 11	1:00	0.0050	1.492
1995 Nov. 21	14:00	2.670	-0.0290

produced by rotating HST images to make the rings horizontal and summing columns of pixels perpendicular to the rings to find the vertically-integrated I/F as a function of r , the horizontal distance from the center of Saturn:

$$\text{VIF}(r) = \int \text{I/F} dz = \sum_z \langle \text{I/F} \rangle_{\text{pix}} \sigma_z. \quad (1)$$

Here, σ_z is the projected vertical dimension of a pixel in the plane of the sky at the distance of the observed rings. $\langle \text{I/F} \rangle_{\text{pix}}$ is the mean reflectance of the rings for that pixel, computed from the brightness of the pixel obtained using the standard HST calibration pipeline, the solar spectrum, and the relative distances of the Earth, Sun, and Saturn. We also subtracted a sky level obtained by averaging the rows of pixels above and below the rings in order to remove significant levels of scattered light from Saturn.

All of the resulting HST profiles are contaminated by light from satellites. Because their orbital motion carries the satellites a significant distance over the course of a single HST visit, it is often possible to remove much of their contribution by median-filtering the profiles for the visit. The profiles extracted from WF3 and PC images are sampled at intervals of 640 km and 290 km/pixel, respectively, and we median filtered all the available profiles of each ansa from each HST visit to produce composite profiles with a resolution of 650 km. If there were only two images of a given ansa in that visit, we took the *minimum* of the two profiles at each pixel as the value for the composite profile. This removes many of the satellites, but fails to remove all traces of bright satellites, satellites near the ansa (where their motion in r is slower), or instances where two or more satellites were close to one another in r . Dips around $r = 105,000$ km in the 25:00 UT profile are due to flux from Mimas, which has a noticeable inclination, and thus contaminates the sky subtraction.

The resulting profiles, published for the first time here, are shown in Fig. 1. When viewed on the dark side (14:00–20:00 UT) and nearly edge-on (22:00 UT), the rings are uniform in brightness out to a radius beyond the outer edge of the A ring (136,800 km) but drop off steeply at the location of the F ring (140,200 km). As originally suggested by Nicholson et al. (1996), this implies that the edge-on brightness is dominated, not by light reflected from the vertical edge of the main rings, as had generally been assumed, nor from the Mimas 5:3 bending wave, but from the F ring. After the ring-plane crossing, the brightness of the main rings increases dramatically.

These profiles were produced to illustrate the variation of VIF with radius. Due to inconsistencies in the calibration between WF3 and PC chips (see Sec. 2.2) and the incomplete removal of flux from satellites, the overall brightness is not well-determined and the asymmetry between the ansae is not clearly shown in these profiles.

2.2. HST $\langle \text{VIF} \rangle$ vs. time

We have reproduced the ring brightnesses measured by Nicholson et al. (1996) by averaging the VIF of the rings over a range of $r = 80,000$ – $120,000$ km, after removing light from the satellites. This $\langle \text{VIF} \rangle$ is plotted vs. time in Fig. 2. The intersection of linear fits to the $\langle \text{VIF} \rangle$ of each ansa before and after

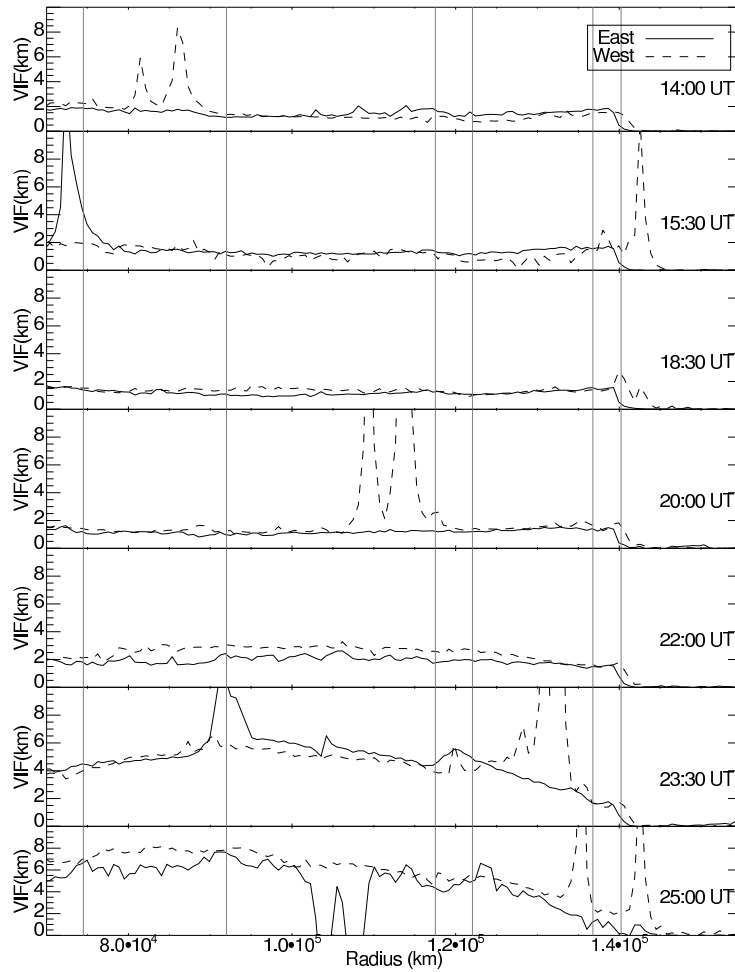


Figure 1: Profiles of $VIF(r)$ extracted from images of the east and west ansae of the rings from HST images taken on 10–11 August 1995. All the profiles are plotted on the same vertical scale. The light from satellites was removed through median or minimum filtering of all the profiles from each ansa in each HST visit, but the remnants of some satellites remain as valleys (where satellite light contaminated the sky subtraction) or peaks. The vertical lines indicate the inner border of the C ring, the boundary between the C and B ring, the inner and outer borders of the Cassini Division, the outer edge of the A ring, and the location of the F ring.

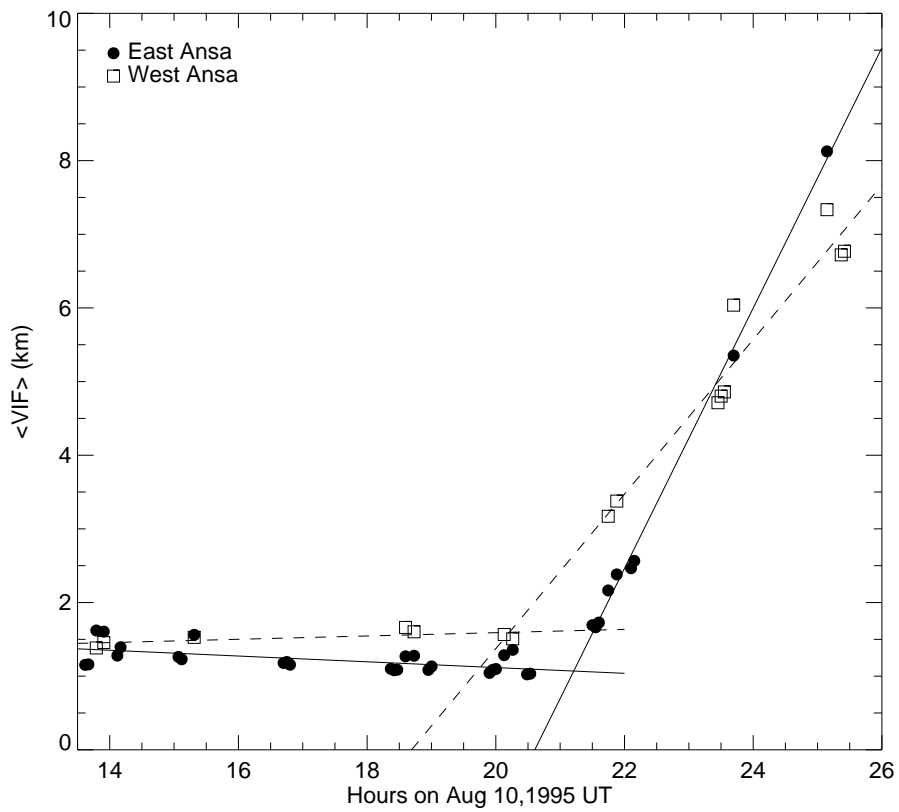


Figure 2: The evolution of the brightness of the rings during the Earth ring-plane crossing of 10 August 1995 as observed by HST. This plot shows data from both WF3 and PC chips, which have been recalibrated (cf. Fig. 2 of Nicholson et al. (1996)). The lines are linear fits to the data from the east and west ansae, before and after the ring-plane crossing. Their intersection gives the ring-plane-crossing time, which we find to be $20:13 \pm 22$ min for the west ansa and $21:13 \pm 3$ min for the east ansa.

Table 2: Average HST visit $\langle \text{VIF} \rangle$ and asymmetries for each visit 10–11 August 1995. Uncertainties were computed from the scatter in data points for each visit, unless only one image was taken.

	UT Time	$\langle \text{VIF} \rangle_E$ (km)	$\langle \text{VIF} \rangle_W$ (km)	$\Delta \langle \text{VIF} \rangle$ (km)
	14:00	1.37 ± 0.19	1.42 ± 0.04	-0.05 ± 0.19
	15:30	1.35 ± 0.15	1.53	-0.18 ± 0.21
Dark	16:30	1.18 ± 0.02	—	—
	18:30	1.15 ± 0.08	1.63 ± 0.03	-0.48 ± 0.09
	20:00	1.13 ± 0.12	1.54 ± 0.03	-0.41 ± 0.12
	22:00	2.09 ± 0.36	3.27 ± 0.10	-1.18 ± 0.37
Lit	23:30	5.35	5.10 ± 0.54	0.25 ± 0.75
	25:00	8.13	6.94 ± 0.28	1.19 ± 0.40

the ring-plane crossing was used to compute the ring-plane-crossing time for each ansa. Uncertainties were calculated from the statistical uncertainties in the fit parameters.

These data were taken with the narrow-band methane filter at 890 nm, which was part of a unique “quad filter” in WFPC2 that was used only infrequently and was rather poorly calibrated at the time of the observations. The figure presented here differs slightly from Fig. 2 of Nicholson et al. (1996) because a photometric calibration factor, which differed slightly between the WF3 and PC images, was not applied correctly to the data plotted in the original work, where all data were mistakenly scaled by the same factor.

The ring-plane-crossing times originally computed from these incorrectly calibrated data by Nicholson et al. (1996) were $20:20 \text{ UT} \pm 8 \text{ min}$ for the west ansa and $21:09 \text{ UT} \pm 2 \text{ min}$ for the east ansa. With the corrected photometric calibration, we find slightly revised ring-plane-crossing times of $20:13 \pm 22 \text{ min}$ for the west ansa and $21:13 \pm 3 \text{ min}$ for the east ansa.

Nicholson et al. (1996) also averaged over all pre-crossing data points and found an average dark side $\langle \text{VIF} \rangle$ of $1.53 \pm 0.09 \text{ km}$ on the west ansa and $1.22 \pm 0.17 \text{ km}$ on the east ansa. It appears that the data used in this calculation were calibrated correctly.

The mean values of the $\langle \text{VIF} \rangle$ of each ansa for each HST visit are given in Table 2. When there is more than one image of an ansa per visit, uncertainties are computed from the scatter in data points. (Nicholson et al. (1996) do not quote any uncertainties for individual measurements.)

Table 2 also gives the asymmetry in brightness between the east and west ansae, defined as

$$\Delta \langle \text{VIF} \rangle = \langle \text{VIF} \rangle_E - \langle \text{VIF} \rangle_W. \quad (2)$$

In the 16:30 UT visit, only the east ansa was imaged, so no asymmetry is given. When the uncertainty can only be computed for one ansa, we estimate the error in the asymmetry in $\langle \text{VIF} \rangle$ by multiplying that error by $\sqrt{2}$.

In Fig. 2, in the observations of the dark side of the rings, $\langle \text{VIF} \rangle_W$, was slightly greater than $\langle \text{VIF} \rangle_E$, with the asymmetry increasing as the RPX approached. It is not clear if the difference in brightness between the ansae is statistically significant before 18:30 UT.

For the first observations after the ring-plane crossing, at 22:00 UT, the west ansa is brighter than the east ansa by 56%. The sense of the asymmetry reverses around 24:00 UT, and in the last set of data, the east ansa is brighter than the west ansa by 16%.

In order to avoid bright satellites, the PC imaged only the east ansa before 23:00 UT and only the west ansa after 23:00 UT, and the relative calibration of the WF3 and PC images remains a matter for concern. For these reasons, we will be comparing our model results only to results from WF3, because these images contain both ansae, and thus the relative calibration between east and west ansae is more certain. Fig. 3 is a plot of $\langle \text{VIF} \rangle$ vs. time including only WF3 images. Computing the RPX times as before, we find the east ansa crossing time to be $21:13 \pm 3 \text{ min}$ and the west ansa crossing time to be $20:25 \pm 10 \text{ min}$. Table 3 gives the asymmetries calculated from the WF3 images alone for each HST visit. Notice that these show that

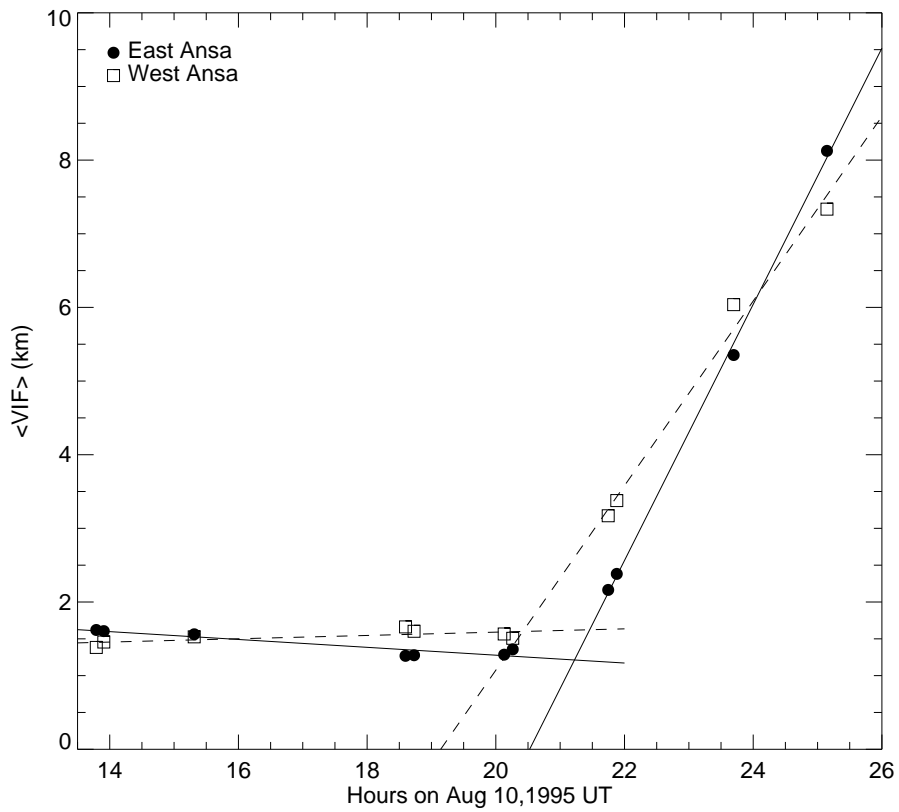


Figure 3: The evolution of the mean brightness of the rings during the Earth ring-plane crossing of 10 August 1995 as observed by HST. This plot shows data from only the WF3 chip (cf. Fig. 2 which contains data from both chips). The lines are linear fits to the data. The intersection of linear fits for each ansa before and after the ring-plane crossing give an estimate of the ring-plane-crossing time. Using WF3 data only, we find the RPX times to be UTC 20:25 \pm 10 min for the west ansa and UTC 21:13 \pm 3 min for the east ansa.

Table 3: Radially averaged VIF for WF3 images only on 10 August 1995.

UT Time	$\langle \text{VIF} \rangle_E$ (km)	$\langle \text{VIF} \rangle_W$ (km)	$\Delta \langle \text{VIF} \rangle$ (km)
14:00	1.61	1.41	0.19
15:30	1.56	1.53	0.03
18:30	1.28	1.63	-0.35
20:00	1.32	1.54	-0.22
22:00	2.27	3.28	-1.01
23:30	5.35	6.04	-0.69
25:00	8.13	7.33	0.80

the *east* ansa is slightly brighter before 16:00 UT, in contrast to Fig. 2 where the west ansa is as bright or brighter than the east ansa at all times before the RPX.

Our model seeks to reproduce both the shapes of the HST profiles in Fig. 1 as well as the asymmetries in Fig. 3.

3. The F ring

3.1. Spacecraft imaging observations of the F ring

The F ring was discovered in Pioneer 11 images, where the F ring’s clumpy nature was immediately apparent (Gehrels et al., 1980). Voyager 1 and 2 revealed up to four strands in the core of the F ring that were braided and kinked at some longitudes (Smith et al., 1981, 1982). Clumps were observed to maintain their integrity for up to 15 orbits around Saturn (Showalter, 2004).

In Voyager Wide-Angle Camera images, the F ring typically varies in brightness by a factor of four with longitude in large part due to phase angle variations, but with comparable variations due to clumping (Showalter et al., 1992).

The Cassini Imaging Science Subsystem (ISS) has obtained complete azimuthal coverage of the F ring, revealing that in the current epoch the F ring has a radial width of ~ 700 km. The F ring has a core with a radial width of ~ 20 km. (Murray et al., 2004).

Longitudinally-complete F-ring observations by ISS at one orbital position revealed that the strands and core of the F ring exhibit complex, temporally evolving structure due to interactions with Prometheus (Kolvoord et al., 1990; Murray et al., 2005; Beurle et al., 2010) and smaller clumps and moonlets in the F-ring region (Barbara and Esposito, 2002). Charnoz et al. (2005) found that the strands of the F ring, as observed November 2004–May 2005, constitute a single spiral arm. This kinematic spiral may have been created by the collision of a kilometer-sized moonlet with the F ring (Murray et al., 2008).

Murray et al. (2008) suggest that there may be larger particles distributed irregularly in the F ring, because moonlets passing through the F ring produce features through impacts, but do not do so with every pass. While they may be in large part responsible for the F-ring’s variable structure, larger objects within the F ring and other moonlets near the F ring do not scatter a large amount of light in the near infrared, and compared to the more extended dusty core and dust envelope, do not contribute significantly to the equivalent depth, as discussed below.

3.2. Occultation measurements of the F ring

The emerging picture of the F ring as revealed by occultation studies is that it consists of a large, diffuse envelope of dusty material with an optically thicker dusty core, sometimes accompanied by dusty strands.

An occultation of the star δ Scorpii by the rings, observed at $0.264 \mu\text{m}$ by the Voyager 2 PPS, yielded a profile of vertical optical depth, $\tau_v(a)$, measured along a line of sight perpendicular to the ring plane, as a function of a , the radial distance from the center of Saturn. In the F-ring, an often-stranded core ~ 3 km

Table 4: Equivalent depths (D) of the F ring measured from stellar occultations in the visible, infrared, and ultraviolet.

Star	Year	B (°)	D (km)	Wavelength	Observatory	References
δ Sco	1981	28.3	4.33±0.13	0.264 μm	Voyager 2	<i>a</i>
			3.79±0.08	3.1 μm	IRTF	<i>b</i>
28 Sgr	1989	25.4	3.0±0.1	3.9 μm	Palomar	<i>b</i>
			2.8±0.1	2.3 μm	MacDonald (ingress)	<i>c</i>
			3.6±0.1	2.3 μm	MacDonald (egress)	<i>c</i>
GSC5249 -01240	1995	-2.67	7.41±0.15	270–740 nm	HST	<i>c</i>
			5.76±0.06	2.3 μm	IRTF	<i>c</i>
Various	2005–8	Various	9.7±	110–190 nm	Cassini	<i>d</i>
Various	2005–9	Various	9.99±2.65	2.92 μm	Cassini	<i>e</i>

^aLissauer et al. (1984); Showalter et al. (1992); Nicholson et al. (1990); Albers et al. (2012)

^bNicholson et al. (2000)

^cBosh et al. (2002)

^dAlbers et al. (2012)

^eHedman et al. (2011); French et al. (2012)

wide had an optical depth ~ 0.5 and ~ 1 in some narrow (< 0.5 km) regions (Lane et al., 1982). In this profile, the envelope extends at least 50 km radially, and the total equivalent depth,

$$D = \int \tau_v(a) da, \quad (3)$$

was measured to be 4.33 ± 0.13 km (Showalter et al., 1992). The ring-opening angle to Voyager during the occultation was 28.3° (Nicholson et al., 1990). This occultation, and those discussed below, are summarized in Table 4.

An occultation of the star 28 Sagittarii was observed from Earth in 1989 at several wavelengths from several observatories when the ring-opening angle was $B_e = 25.4^\circ$. An equivalent depth at $\lambda = 3.1 \mu\text{m}$ of 3.79 ± 0.08 km was measured from observations at the Infrared Telescope Facility (IRTF), and an equivalent depth of 3.0 ± 0.1 km was observed at $\lambda = 3.9 \mu\text{m}$ at Palomar Observatory (Nicholson et al., 2000). Two separate equivalent depths were obtained at MacDonald Observatory at $\lambda = 2.3 \mu\text{m}$: $D = 2.8 \pm 0.1$ km at ingress and 3.6 ± 0.1 km at egress, highlighting the azimuthal variation in the F ring (Bosh et al., 2002).

In 1995, very close to the solar ring-plane crossing ($B_e = -2.67^\circ$), an occultation of the star GSC5249-01240 was observed by HST using the Faint Object Spectrograph at wavelengths of 270–740 nm. The F ring’s equivalent depth was measured to be 7.41 ± 0.15 km. Simultaneous observations at IRTF at $\lambda = 2.3 \mu\text{m}$ yielded an equivalent depth of 5.76 ± 0.06 km (Bosh et al., 2002).

The Cassini Visual and Infrared Mapping Spectrometer (VIMS) has observed 87 stellar occultations by the F ring. Integrating over a radial range of 150 km, Hedman et al. (2011) find an average equivalent depth at $3.2 \mu\text{m}$ of 6 km, with a standard deviation of 3 km. A subset of 30 of these occultations were analyzed over a larger radial range of 600 km of radial extent by French et al. (2012), who found an equivalent depth of 9.99 ± 2.65 km at $2.92 \mu\text{m}$.

Some observations reveal isolated regions with higher optical depths. These regions may be composed of larger ring particles, and some optically thick spikes in occultation profiles may be moonlets.

Occultations observed by the Cassini Ultraviolet Imaging Spectrograph (UVIS) showed highly variable profiles with several features of higher optical depth with radial widths of up to 1.4 km, including sharp-edged features that may be temporary aggregations of smaller bodies and one opaque feature that could be a moonlet (Esposito et al., 2008), and Albers et al. (2012) detect a wake that is consistent with a moonlet embedded in the F ring. UVIS observations show that the core usually has a U-shaped radial profile but sometimes has V- or even W-shaped profiles (Meinke et al., 2010). A comprehensive analysis of UVIS occultations from 2005–2008 yields an average peak optical depth of 0.43 in the core, and equivalent widths of the entire F ring ranging from 3.9–50.8 km, with average of 9.7 km (Albers et al., 2012).

Radio occultations are sensitive to larger ring particles only, and the parts of the F ring comprising only small dusty particles are not detected. Only a compact region with a width of < 1 km was seen the Voyager 1 Radio Science Subsystem occultations at $\lambda = 3.6$ cm and 13 cm, implying that the larger dusty portion of the F-ring core, not detected in the radio, is composed of particles with sizes much less than $\lambda/3 \sim 1$ cm (Marouf et al., 1986). Showalter et al. (1992) measured equivalent depths from the Voyager profiles of 0.283 ± 0.035 km and 0.153 ± 0.066 km at $\lambda = 3.6$ and 13 cm, respectively. These equivalent depths may be a slight underestimate because no measurable intensity passed through the densest part of the core, a region ~ 300 m wide (Marouf et al., 1986), but they are small compared to the equivalent depths of the dusty F-ring component in the infrared. This region is absent in 14 of 25 Cassini Radio Science Subsystem (RSS) occultation profiles at 0.94 and 3.6 cm, and present in only 3 occultations at 13 cm. When present in the RSS occultations, the F ring is 1 km wide with a peak optical depth of ~ 0.1 (Marouf et al., 2010).

Spectral analysis of VIMS occultations show that regions of higher optical depth tend to have smaller fractions of small particles, i.e. they are composed of larger particles than the rest of the dusty ring (Hedman et al., 2011). These large-particle regions are not obvious in imaging, and it is difficult to characterize their longitudinal extent because occultations give us information about only an isolated cut through the F ring. They may be interpreted as a “discontinuous core” (see, e.g. Marouf et al. (2010)) or as isolated regions.

Though the optical depths of such regions is higher (and moonlets are, of course, opaque), they tend to be narrow in radial extent. We therefore do not expect them to make a large contribution to the blocking efficiency of the F ring, and it is probably the dusty regions (including the dusty core) that dominate the F-ring equivalent depth.

3.3. Comparing different measurements of equivalent depth

Because the F ring is largely optically thin, the assumed geometry has little effect on the measured equivalent depth. Consider a ring extending radially in the ring plane from $a = r_0$ to $a = r_1$ and vertically a distance z_o above and below the ring plane. Let the ring’s opacity be described by some function $\kappa(a, z)$, while its mass density is $\rho(a, z)$.

In an occultation, the intensity of a star, I_o , is attenuated to $I = I_o e^{-\tau_v/\mu}$, where τ_v is the normal optical depth, and $\mu = \cos B$, where B is the ring-opening angle to the observer. An observer directly above the ring plane ($B = 90^\circ$) observing an occultation of a star passing below the rings measures the vertical optical depth τ_v as a function of radius, a . The optical depth is defined in terms of the absorption coefficient:

$$\tau_v(a) = \int_{-z_o}^{z_o} \kappa(a, z) \rho(a, z) dz. \quad (4)$$

The equivalent depth is

$$D = \int_{a_0}^{a_1} \tau_v(a) da \quad (5)$$

$$= \int_{a_0}^{a_1} \int_{-z_o}^{z_o} \kappa(a, z) \rho(a, z) dz da. \quad (6)$$

Consider now an observer of an RPX, who looks radially inward at the ring from a position in the ring plane ($B = 0^\circ$). Such an observer measures the radial optical depth, $\tau_r(z)$. Integrating along the line of sight to the star through the F ring,

$$\tau_r(z) = \int_{a_0}^{a_1} \kappa(a, z) \rho(a, z) da. \quad (7)$$

The vertical analog to equivalent depth is then

$$D' = \int_{-z_o}^{z_o} \tau_r(z) dz \quad (8)$$

$$= \int_{-z_o}^{z_o} \int_{a_0}^{a_1} \kappa(a, z) \rho(a, z) da dz = D. \quad (9)$$

Table 5: F-ring orbital parameters from Bosh et al. (2002) for the pole of French et al. (1993).

a	140223.7 ± 2.0 km
$e \times 10^3$	2.53 ± 0.06
ϖ^a	$24.1 \pm 1.6^\circ$
$\dot{\varpi}$	$2.7001 \pm 0.0004^\circ/\text{day}$
i	$0.0064 \pm 0.0007^\circ$
Ω_o^a	$17.3 \pm 3.9^\circ$
$\dot{\Omega}$	$-2.6877^\circ/\text{day}$

^aLongitudes are measured from the intersection of Saturn’s equatorial plane with the Earth’s equatorial plane. The reference epoch is J2000.0=JD 2451545.0.

We see that these orthogonal equivalent depth measurements are identical for an optically-thin ring, as long as the line of sight is corrected to the radial direction and integration is vertical, or the line of sight is corrected to normal to the ring plane and the integration is radial, as the case for these observations (Bosh et al., 2002; Nicholson et al., 2000; Showalter et al., 1992).

If a ring is optically thick (i.e., $\tau/\mu \gg 1$) then when we attempt to measure the attenuated intensity, we will simply find that $I = I_o e^{-\tau/\mu}$ approaches 0. Thus, we can only find the lower limit for τ , and thus D, based on the limit of sensitivity of the detector. However, if a ring is optically thin (i.e., $\tau/\mu < 1$) in all of our observations, as is largely true for the F ring in the infrared, we will always be able to measure some intensity and can calculate the true value of τ . Whenever we are looking at the same piece of ring, we will calculate the same D whether we view the ring from above, or the side, or from any intermediate angle.

3.4. The inclination of the F ring

Using data from several stellar occultations, including one observed near the time of the solar RPX in November 1995, Bosh et al. (2002) created a kinematic model of the F ring that includes both an eccentricity and an inclination. We use their Fit #3, which was computed using the Saturn pole of French et al. (1993). For reference, the orbital parameters are listed in Table 5.

At its highest point, the F-ring plane rises $a_f \sin i_f = 16$ km above the main-ring plane, and it dips below the ring plane by the same amount. Compared to the ~ 350 km radial excursions of the ring due to its eccentricity, this vertical displacement is very small. However, the tilt of the ring becomes important when the ring-opening angle is small enough that the projected height of the main rings on the sky is comparable to the F ring’s vertical displacement. For example, at an Earth ring-opening angle of $B_e = 0.0050^\circ$, ~ 4 hours from the exact moment of RPX on 10 August 1995, the total projected height of the main rings, whose outer radius is $R = 137,000$ km, is only $2R \sin B_e = 24$ km, comparable to the F ring’s vertical displacement.

If the F ring’s line of nodes is neither parallel nor perpendicular to the line of sight, then the front of the F ring obscures one ansa of the main rings more than the other. Conversely, the main rings block more of the back of the F ring on one ansa than on the other.

4. The photometric model

4.1. The Poulet model

In order to reproduce the observed brightness of the rings of Saturn in the near-infrared during the 1995 Earth ring-plane crossings, Poulet et al. (2000) constructed a photometric model of the rings in which the F ring was the most important contributor to the brightness of the rings close to the ring-plane crossing. This model (hereafter referred to as the Poulet model) was created to reproduce observations of the dark side of the rings from the University of Hawaii 2.2-m telescope on 22–23 May 1995, from the European Southern Observatory (ESO) 3.6-m telescope at La Silla, Chile on 9–10 August, and of the lit side of the rings from the Pic du Midi 2-m telescope on 12–13 August. Observations of both the dark and lit sides

of the rings from HST on August 10–11 were also analyzed, but no attempt was made to reproduce the east-west asymmetry in brightness.

In the Poulet model, the F ring was treated as a uniform uninclined toroid of rectangular cross-section. Based on the shape of profiles extracted from the images of the dark side of the rings near the RPX, where the light contributed by the main rings was minimized, Poulet et al. (2000) derived an F-ring vertical optical depth of $\tau_v \sim 0.16 \pm 0.05$ from the HST data ($\lambda=0.89 \mu\text{m}$), 0.19 ± 0.05 from the Hawaii data ($\lambda=2.2 \mu\text{m}$), and 0.27 ± 0.10 from the ESO data ($\lambda=2.15 \mu\text{m}$).

For the HST data, Poulet et al. (2000) found the best fit to the data with a physical height of the F-ring model of $H = 21 \pm 4$ km, with an equivalent depth of $D=8 \pm 3$ km. This value is larger in general than the early equivalent depths obtained from occultation data, but agrees with more recently-measured equivalent depths (see Table 4).

To fit the phase behavior of the F ring (albeit over a range of only $\alpha = 3.55\text{--}5.55^\circ$), the Poulet model employed a dust component and a macroscopic component. The fraction of the F-ring brightness contributed by dust in the model ranged from 0.8–0.9.

4.2. A new ring model

While reproducing the observed overall edge-on brightness of the rings, the uninclined F ring of the Poulet model cannot explain the difference in brightness between the east and west ansae observed in HST images of the August 10 RPX seen in Figs. 2 and 3. In Fig. 4, a very simple cartoon shows that during this particular ring-plane crossing, the F ring’s inclination causes it to obscure, and be obscured by, the main rings by differing amounts on the east ansa and west ansa. In particular, immediately after the RPX, the east ansa is more obscured by the F ring, then an hour and a half later (as the Earth passes through the F ring’s plane) the obscuration is similar, and finally the west ansa is covered by the F ring. This qualitative picture agrees with the asymmetries in brightness observed after the ring-plane crossing, shown in Fig. 2, where immediately after the RPX the brightness of the east ansa is less than that of the west ansa, then the brightnesses are similar, and then the east ansa is brighter than the west ansa.

In Fig. 4, the F ring’s height was arbitrarily chosen to be 10 km, but clearly the vertical extent and structure of the F ring will affect the degree of asymmetry observed at different times. Thus the brightness asymmetry at ring-plane crossing gives us an opportunity to probe the properties of the F ring perpendicular to the usual radial dimension, which has been well-studied in spacecraft imagery and stellar occultation data.

Our major improvements over the Poulet model, then, are to include the inclination of the F ring and to use a more realistic vertical profile of the F ring’s structure. Unlike Poulet et al. (2000), we do not address the particle size in the F ring, because of the limited phase coverage of the HST data.

The components of our photometric ring model are: the F ring, divided into a front half and a back half, and the main rings of Saturn (including the A, B and C rings, and the Cassini Division).

The resolution of our model images is 600 km per model pixel in the horizontal direction (similar to the resolution of the HST WF3 images) and ~ 0.03 km in the vertical direction. The images are stretched vertically by a factor of $\sim 18,500$ in order to correctly model the F ring’s obscuration of the major features in the main ring (the narrowest of which is the Cassini Division). An image size of 500×4000 pixels was chosen to accommodate the vertical extent of the F ring during all the model times. The F-ring model is constructed as a cylindrical band composed of rectangular cells that are $\sim \frac{1}{4}$ the size of the pixels in the model image. (For a detailed discussion of the model resolution, see Appendix A.1 and Fig. A.11).

For comparison with the HST observations, we model the ring brightness at the rounded visit times: 14:00, 15:30, 18:30, 20:00, 22:00, 23:30, and 25:00 UT. There was little systematic variation in the brightness of the rings in the two WF3 images taken during each dark side visit, when the rate of change in brightness is small. In the last two visits on the lit side of the rings, there is only one WF3 image, which fell very near this rounded time. Only during the 22:00 visit were two images taken, and there was a significant, systematic change in the brightness at these two times. However, the brightness of the two ansae increase at roughly the same rate, so this has little impact on the asymmetry measurement. It does lead to a discrepancy in overall brightness between our model profiles and the observed profiles, as discussed in Sec. 5.2.2.

The model consists of several image layers at each model time, with the value of each pixel in each layer representing the pixel’s area-integrated I/F (AIF). The AIF is then summed over the entire vertical column

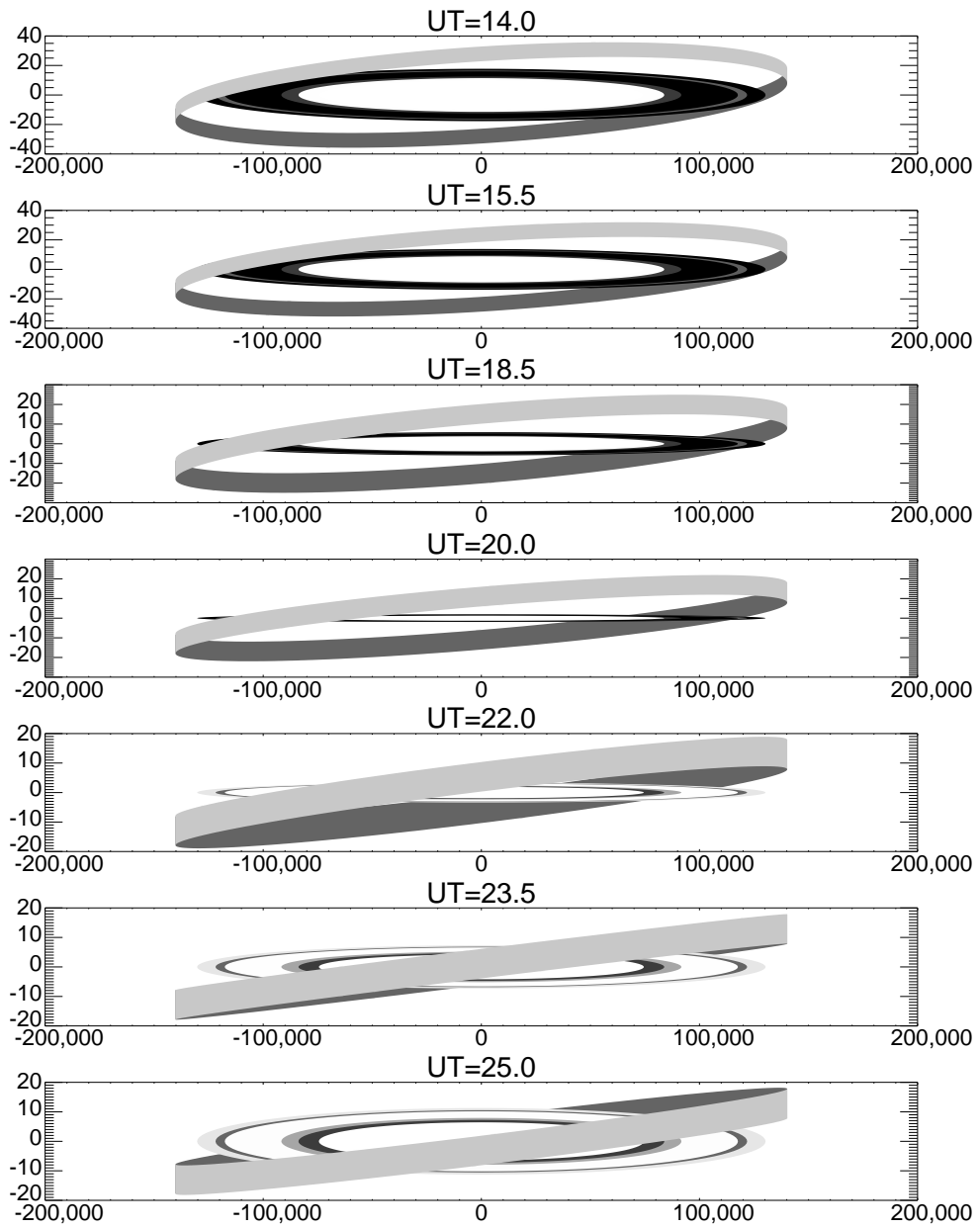


Figure 4: Diagrams showing the geometry of the rings at each of the HST observation times. The total vertical thickness of the F ring was arbitrarily set to 10 km in these diagrams. The Earth crosses the plane of the main rings at $\sim 21:00$ UT and the plane of the F ring at $\sim 23:30$ UT.

Table 6: Single-scattering albedos for the main rings based on 0.5- μm Voyager observations.

Ring Region	Inner Radius (kkm)	Outer Radius (kkm)	Single-Scattering Albedo ^a	Reference
C ring (inner)	74.5	83.9	0.18	Cooke (1991)
C ring (outer)	83.9	91.7	0.31	Cooke (1991)
B ring	91.7	117.6	0.66	Doyle et al. (1989)
Cassini Division	117.6	121.9	0.38	Smith et al. (1981)
A ring	121.9	136.9	0.6	Dones et al. (1993)

^aScaled up by a factor of 1.2 based on the ring spectra of Karkoschka (1994) at $\lambda=0.5$ and $0.89 \mu\text{m}$.

of the image layer and divided by the pixel width to find the VIF. Finally, the VIF is averaged over 80,000–120,000 km, the same radial range used to calculate the $\langle\text{VIF}\rangle$ in Fig. 2 and Table 2 and Nicholson et al. (1996).

4.3. The model of the main rings

Table 1 shows ring-opening angles to the Sun and Earth, B_s and B_e , calculated separately for each visit and interpolated from ephemerides provided by the Planetary Data System’s Rings Node (<http://pds-rings.seti.org>). The right ascension and declination of Saturn, α_s and δ_s , were also obtained from this ephemeris for use in the calculation of the orientation of the F ring.

The normal optical depth of the main rings as a function of radial distance from the center of Saturn was measured in ground-based observations of the occultation of the star 28 Sgr by Saturn’s rings in 1989 (Nicholson et al., 2000). We use the optical depth profiles derived from the data taken with the Lick 1-m Nickel reflector at a wavelength of $0.9 \mu\text{m}$ because these observations are of consistent quality and are at nearly the same wavelength as the HST observations (French et al., 2003). We use only the egress data, as the ingress data are noisier due to thin clouds over the observing site. (This profile is plotted in Fig. A.12.)

To calculate the reflectance of the main rings we also require the single-scattering albedo of the different regions of the rings and the phase factor (which we will take to be the same for all parts of the rings). Because these photometric parameters, especially the albedo, are not well-known in the near infrared, we will begin with provisional values, which will be rescaled in the course of modeling.

The nominal single-scattering albedos used in the main-ring model, listed in Table 6, are derived from Voyager clear-filter observations. For our model, which seeks to reproduce the ring brightness at $0.89 \mu\text{m}$, we have scaled these albedos up by a factor of 1.2, based on the full-ring spectrum of Karkoschka (1994). We neglect small differences in the spectra of the different regions of the rings.

We employ a Callisto-type phase function (Dones et al., 1993) for all regions of the main rings. The I/F of the rings is then computed using the standard single-scattering reflectance formulae from Chandrasekhar (1960), as described in Sec. Appendix A.2.

We have also calculated the contribution of saturnshine to the brightness of the main rings. Our saturnshine model was tested by reproducing the observed brightness profile in an image from the Sun ring-plane crossing on 21 November 1995, including an east-west asymmetry that was noted by Nicholson et al. (1996), which is caused by the relatively large phase angle at that time. Because the 10–11 August solar ring-opening angle is much larger than in that November, we find that directly reflected and transmitted sunlight is much brighter than the saturnshine, and that saturnshine can safely be neglected in modeling the data in Figs. 1 and 3. The calculation of saturnshine is discussed in detail by Scharringhausen (2007), and a profile of brightness for 21 November 1995 is given in Fig. A.13

4.4. The F-ring model

The F ring is constructed as a two-dimensional array of 6000×6000 cells, with a vertical height of $h_f=60$ km, arranged as an inclined “ribbon” in three dimensions. We calculate the sunlight scattered by

the F ring as well as the amount of light from the main rings and from the back of the F ring that is blocked by the front of the F ring.

The physical radial width of the F ring, ~ 50 km, being much smaller than the semimajor axis, has very little impact on the photometric model. Also, the only effect of the eccentricity would be a radial displacement of at most $a_f \cdot e_f = 350$ km of the F ring at the ansa, which is less than the 600-km horizontal resolution of the main-ring model. We therefore take the radius of the F-ring model, equal to $a_f = 140,200$ km (Bosh et al., 2002), as a constant for all cells.

Each cell in the F ring is assigned a *radial* optical depth according to the formula

$$\tau_r(h) = \tau_o e^{-(h/h_o)^2}, \quad (10)$$

where h is the height above the mean F-ring plane, τ_o is the radial optical depth at the midplane, and h_o determines the width of the vertical profile of the optical depth. τ_o and h_o are the two major parameters in our photometric model.

The brightness of the F ring is also calculated using the single-scattering equations of Chandrasekhar (1960), as applied to our model of a vertical ribbon wrapped around Saturn. As the light from the back of the F ring and from the main rings passes through the front of the F ring, its intensity will be reduced by a factor of $e^{-\tau_{los}}$, where $\tau_{los} = \tau_r(h)/\cos(\theta)$ is the optical depth along the line of sight. Here, θ is the angle between the local radial direction and the line of sight to Earth, which varies from $-\pi/2$ to $\pi/2$. Both calculations are described in Section Appendix A.3.1.

4.5. Albedo scaling

Here we summarize the rescaling of F-ring and main-ring model brightnesses to match the observations. This process is discussed in more detail in Sec. Appendix A.3.2.

Because the albedo and phase factor of the F ring at the wavelength of this observation is not well-known, we determine it empirically. Before the ring-plane crossing, the amount of sunlight reflected by the main rings is small compared to the sunlight reflected from the F ring. When the model is first run, the factor $P(\alpha)\varpi_o$ for the F ring is set to 1. The resulting dark-side (pre-RPX) model brightness is compared to the observed HST \langle VIF \rangle , averaged over all dark-side times, and a constant scaling factor $p_f = P(\alpha)\varpi_o$ is used to re-scale the brightness of the F-ring model so that it matches the observed brightness. We recompute this factor for each set of parameters h_o and τ_o , as discussed below.

The albedos of the main rings at $0.89 \mu\text{m}$ are also not well-determined. We run the model with the nominal albedos and phase factors from Table 6, then rescale the brightness of the main rings by a single factor p_m at all times so that the model \langle VIF \rangle s match the brightness observed in the HST observations *after* the ring-plane crossing for each set of model parameters. This preserves the main ring profile's shape, which depends on the optical depth profile of the rings and the relative albedos of the different regions, while allowing us to correct empirically for uncertainties in the main ring single-scattering albedos in the near infrared.

4.6. F-ring model parameters

Besides the albedo scaling factors for the main ring and F ring, which are calculated in the course of the model run, there are two fundamental parameters that are independently varied in this model: τ_o and h_o , which characterize the F ring's vertical optical depth profile *via* Eq. 10. The full width (actually, height) at half maximum (FWHM) of the vertical profile is given by $2\sqrt{\ln 2} h_o = 1.665 h_o$. In addition to these two parameters, it is also convenient to consider the model ring's equivalent depth, D . For our optical depth profile,

$$D = \int_{-30 \text{ km}}^{30 \text{ km}} \tau_r(h) dh = \int_{-30 \text{ km}}^{30 \text{ km}} \tau_o e^{-(h/h_o)^2} dh = \sqrt{\pi} \tau_o h_o \operatorname{erf}\left(\frac{30 \text{ km}}{h_o}\right), \quad (11)$$

where $\operatorname{erf}(x)$ is the error function. Because the equivalent depth has been measured in the F ring in occultations (see Sec. 3.2) we will use D to represent the total amount of matter in the F ring, while h_o

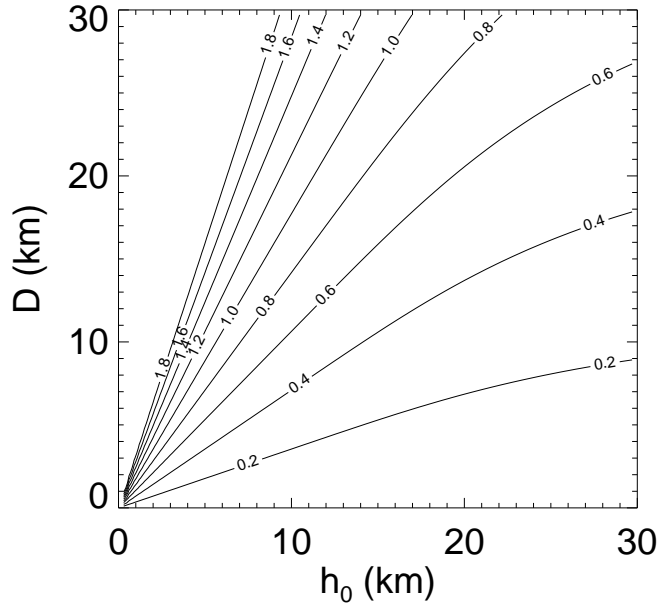


Figure 5: A contour plot of τ_o for a range of values of h_o and equivalent depth.

describes its vertical distribution, and not refer further to τ_o . A contour plot of the values of τ_o for a range of D and h_o is shown in Fig. 5.

Several Gaussians of equal equivalent depth are shown in Fig. 6. A profile with uniform τ , as in the Poulet model, is shown for comparison. Notice that the profiles are cut off at $|h|=30$ km, as in our F-ring model. The larger h_o is, the flatter the profile.

The choice of model parameters is constrained somewhat by the known characteristics of the F ring. As previously discussed, in pre-Cassini occultation events, the equivalent depth has been measured to be between ~ 3 and 8 km at infrared wavelengths. The best-fitting Poulet model had an equivalent depth of 8 ± 3 km. There are no direct constraints on h_o from previous observations, either Voyager imaging or stellar occultations, but a plausible assumption is that the FWHM vertical thickness is not significantly greater than the radial width of the F ring's dusty core, or 20–50 km (Lane et al., 1982; Showalter et al., 1992; Bosh et al., 2002), so that we should expect $h_o \lesssim 50 \text{ km} / 1.665 = 30$ km.

In summary, the variable parameters in the present model are p_f , the product of the albedo and phase factor of the F ring; p_m , a scaling factor for the albedos and phase factor of the main rings; D , the equivalent depth of the F ring; and h_o , a parameter related to the full height at half maximum of the F ring. Whereas p_m and p_f control the overall brightness of the model and are adjusted to match the observed brightness of the rings, D and h_o primarily affect the asymmetry and the shape of radial profiles of I/F (Fig. 1).

For each model run, we chose a pair of h_o and D values. Small values of h_o have a tendency to increase the modeled brightness asymmetries, as the F ring is more concentrated at the core where it falls across the main rings. Large values of D , by increasing the overall amount of blockage by the F ring, also tend to increase the model asymmetries unless the value of h_o is also large.

As discussed in Sec. 4.5, p_f and p_m are computed for each model run, i.e. for each pair of h_o and D , in order to bring the overall model brightness into agreement with the observed brightnesses. For small values of D , p_f must be large so that the model F ring is bright enough to match the observed pre-RPX brightness of the rings, but p_f depends only weakly on h_o . In general, p_m increases as h_o and D increase, because these factors increase the blocking of the F ring, requiring the main rings to be brighter to reproduce the

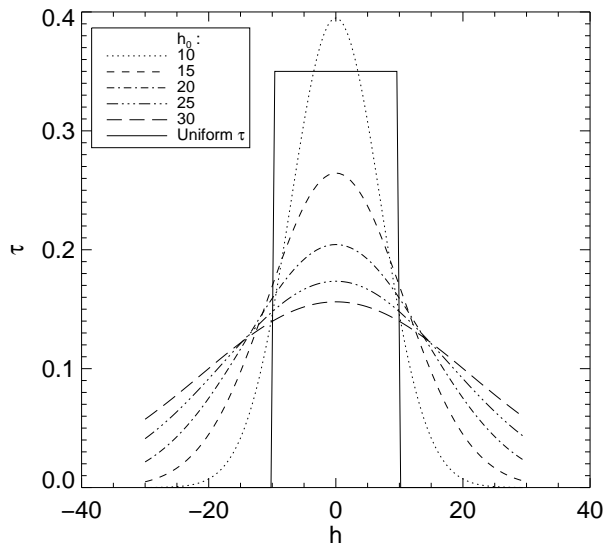


Figure 6: Models of the radial optical depth of the F ring as a function of height above and below the mean F-ring plane, with varying values of h_o and D . The models are cut off at $h=-30$ and $+30$ km. Also shown is a flat profile with a total height of 21 km, similar to the F ring in the Poulet model. The maximum optical depth of each profile, including the flat profile, was chosen so that it has an equivalent depth of 7 km.

observed brightness.

5. Results

We explored the parameter space of h_o and D to find the combination of these parameters that best fit the observed lit-side asymmetry in the HST dataset.

5.1. Best-fitting model

Because we chose the factor p_f for the F ring to match the observed $\langle \text{VIF} \rangle$ on the dark side and p_m for the main rings to match the observed $\langle \text{VIF} \rangle$ on the lit side, the overall model brightness will always be similar to the HST measurements. As will be discussed in Sec. 5.3, there is poor agreement between the model and the small pre-RPX asymmetries; whatever mechanism is responsible for these asymmetries is clearly not reproduced by the model. Therefore, we assess each trial model with a chi-square fit to the lit-side asymmetries, where the asymmetries are expressed as the difference in $\langle \text{VIF} \rangle$ between the east and west ansae at each HST visit. For each (h_o, D) , we compute an unweighted χ^2 ,

$$\chi^2 = \sum_t (\Delta \langle \text{VIF} \rangle_t - \Delta \langle \text{VIF} \rangle_{\text{HST},t})^2, \quad (12)$$

where the sum is taken over only the lit-side model times. A contour plot showing the values of χ^2 that result from models with a range of h_o and D is shown in Fig. 7. The minimum unweighted chi-square is $\chi_{\text{min}}^2 = 0.26 \text{ km}^2$, which is obtained for $h_o = 8 \text{ km}$ and $D=10 \text{ km}$, corresponding to $\tau_o = 0.7$.

It would be preferable to use a weighted chi-square that takes into account the standard deviations for each data point, σ_t :

$$\chi_w^2 = \sum_t \left(\frac{\Delta \langle \text{VIF} \rangle_t - \Delta \langle \text{VIF} \rangle_{\text{HST},t}}{\sigma_t} \right)^2 \quad (13)$$

(Press et al., 1992), but Nicholson et al. (1996) do not quote standard deviations for their $\langle \text{VIF} \rangle$ s. Uncertainties for the HST asymmetries based on the scatter of the HST measurements for each visit are given in Table 2, but it must be stressed that these include both WF3 and PC images, whereas $\Delta \langle \text{VIF} \rangle_{\text{HST}}$ is computed from WF3 images only. Because there are only one or two images WF3 images per visit, we use the errors derived from the scatter in the WF3 and PC images together, which are of order 0.5 km, to serve as an indicator of the general level of uncertainty in the HST measurements. The uncertainties are dominated by the effects of superimposed satellites and F-ring clumps, rather than statistical (i.e., photon) noise.

Lacking rigorous standard deviations for the data, we can assume that a typical uncertainty in the HST asymmetries is represented by σ , so that

$$\chi_w^2 = \frac{1}{\sigma^2} \sum_t (\Delta \langle \text{VIF} \rangle_t - \Delta \langle \text{VIF} \rangle_{\text{HST},t})^2, \quad (14)$$

or

$$\chi_w^2 = \frac{\chi^2}{\sigma^2}. \quad (15)$$

The minimum of a weighted chi-square for a reasonable model fit should be approximately equal to the degrees of freedom. Because we use the three lit-side data points to determine the two model parameters, we should have $\chi_{w,\text{min}}^2 = 1$ (Press et al., 1992). This suggests that $\sigma = \sqrt{\chi_{\text{min}}^2/1} = 0.5$ km, which is in good agreement with the estimated HST uncertainties (on the lit side) in Table 2. As a test, we also computed a weighted χ^2 statistic using the errors on ΔVIF for each HST data point from Table 2 and Eq. 13. The results are not very different from the unweighted χ^2 , yielding the same best-fit parameters, and contours of $\chi_w^2 \sigma^2$ were very similar to contours of χ^2 . Therefore we take 0.5 km to be a good estimate for σ in order to find the uncertainties in our fitted parameters. For a fit with one degree of freedom, the one standard deviation uncertainty in a single parameter is determined by projecting the region where $\chi_w^2 - \chi_{w,\text{min}}^2 = 1$ onto the axis of that parameter (Press et al., 1992). Again, for one degree of freedom, $\chi_{w,\text{min}}^2 = 1$, so $\chi_w^2 = 2$, and using Eq. 15, we find that the uncertainty is defined by the contour where:

$$\chi^2 = 2\sigma^2 = 0.5 \text{ km}. \quad (16)$$

Fig. 7 shows how we project the boundaries of the region where $\chi^2 \leq 0.5$ km onto each parameter's axis. Unfortunately, solutions with $\chi^2 \sim 0.5$ km exist in a large region of parameter space for large values of D and h_o . In this part of the parameter space, the optical depth profile of the F ring is nearly flat, with the overall height set by our model limits of ± 30 km, and there is little to differentiate between the models as h_o and D increase. To estimate the uncertainties of the parameters, then, we ignore this region and use the better-constrained low- h_o side of the $\chi^2 = 0.5$ -km contour. This gives us one-sigma uncertainties of $\sigma_{h_o} = 4$ km and $\sigma_D = 4$ km.

For our best-fit model, $p_f = P(\alpha)\varpi_o = 0.36$. This parameter is largely determined by the $\langle \text{VIF} \rangle$ values measured on the dark side of the rings. Poulet et al. (2000) do not quote values for $P(\alpha)\varpi_o$, but based on their plotted results, we estimate that the fitted value for their final model was ~ 0.6 . However, the Poulet model assumed that the back of the F ring lay entirely hidden behind the front. Our model shows that, especially before the ring-plane crossing, significant parts of the back of the F ring are unobstructed by the front of the F ring, effectively doubling the visible area of the ring. Thus, we are in agreement with the brightness of the ring in the Poulet model because our F-ring area is twice as large but our reflectivity is half as large.

We find that for our best-fit model, our main-ring scaling factor is $p_m \sim 0.7$, so the main rings are about 70% as bright as predicted by single scattering using the nominal photometric parameters. This does not seem unreasonable, considering the uncertainty in the scattering behavior of the main rings at extremely low ring-opening angles and, to a lesser extent, in the spectrum of the ring in the near infrared.

5.2. Radial profiles

Profiles extracted from the different component images in the best-fit photometric model illustrate the time-varying contributions of the main rings and F ring to the total profile. These component profiles and

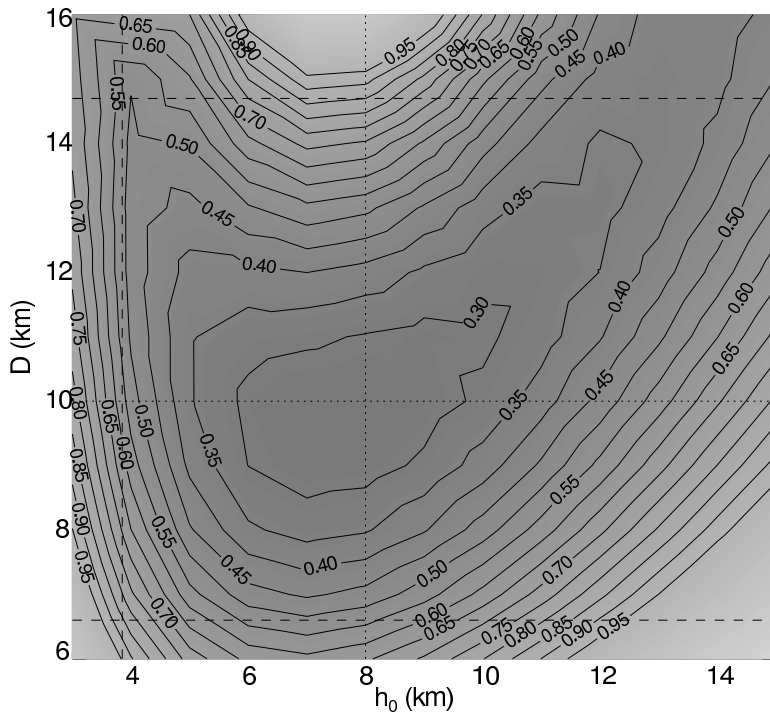


Figure 7: Unweighted χ^2 values for a range of values of model parameters h_o and D . The dotted lines indicate the position of the best fit, for $h_o = 8$ km and $D=10$ km. The dashed lines show the projection of the $1\text{-}\sigma$ contour, where $\chi^2=0.5$ km, onto the h_o and D axes. Because this contour does not close at the upper right, we use the bounds at the lower and left-hand sides to characterize the uncertainty in the model parameters.

total profiles are shown along with diagrams depicting the geometry of the rings in Fig. 8. Profiles of $VIF(r)$ from the best-fit photometric model ($h_o = 8$ km, $D=10$ km) are over-plotted with HST profiles in Fig. 9.

5.2.1. Dark-side profiles

The model profiles are a fair match to the generally flat shape of the HST profiles on the dark side of the rings (i.e., 14:00–20:00 UT). The sunlight reflected from the F ring dominates the model brightness, contributing $VIF \sim 1.5$ km for each ansa.

On both ansae, the model profiles slope upward toward the ansa with a shape typical of a narrow, optically thin ring. However, the HST profiles are flatter at the ansae. For an optically thick narrow ring, the I/F would not increase toward the ansa because τ/μ would always be $\gg 1$, so, using the single-scattering expression for reflected light from Chandrasekhar (1960), in the optically thick limit,

$$I/F \approx \frac{1}{4}P(\alpha)\varpi_o \frac{\mu_o}{\mu + \mu_o} \approx \frac{1}{4}P(\alpha)\varpi_o \frac{1}{\mu/\mu_o + 1} \approx \frac{1}{8}P(\alpha)\varpi_o, \quad (17)$$

leads to a profile that is flat all the way out to the ansa. The flatter HST profiles could therefore be consistent with an optically thick layer of larger particles in the F-ring plane and a more diffuse envelope, suggesting a possible direction for future models.

Prior to RPX, the main rings are dark, and most of the blocking by the front of the F ring, represented by the solid line of negative values in Fig. 8, is of the reflected sunlight from the back of the F ring. This blocking is symmetric east-to-west, and increases as the optical depth along the line of sight increases toward each ansa of the F ring.

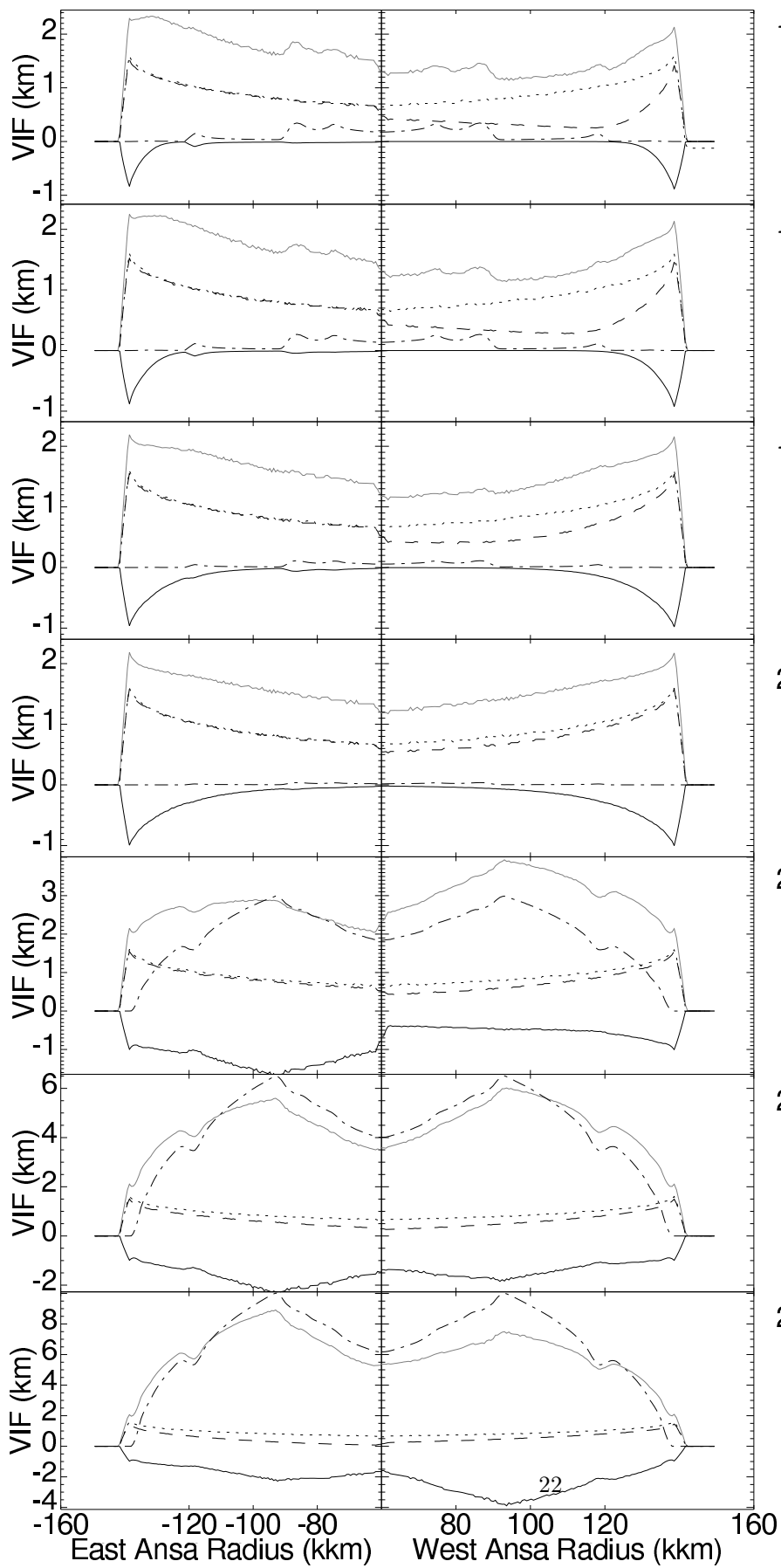
The small asymmetry in the model arises from the blocking of the back of the west ansa of the F ring by the main rings, as can be seen by comparing the east and west dashed profiles in Fig. 8. This blocking decreases as the ring-opening angle decreases, decreasing the projected area of the main rings and is essentially zero at 20:00 UT, at which point, the HST profiles are also symmetrical.

In the HST images, the asymmetry between the ansae is smaller than in the model and the west ansa is slightly brighter than the east ansa at 18:30 and 20:00 UT (cf. Fig. 3), opposite to the sense of the asymmetry caused by blocking of the F ring by the main rings. The model does not reproduce this observed asymmetry, and the HST profiles do not clearly show the asymmetry predicted by the model due to the blocking of the back of the F ring on the west ansa by the main rings. This blocking, which amounts to $\lesssim 0.5$ km of the total VIF, may simply be lost in the “noise” of the actual F ring’s well-known azimuthal variation.

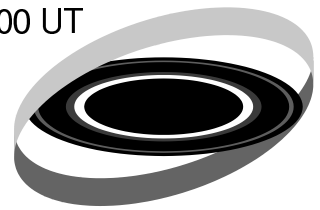
In the model profiles at 14:00 and 15:30 UT, the transmitted light from the C ring contributes a VIF of ~ 0.2 km and is visible interior to 90,000 km, a feature visible in the HST profiles as well. The C ring’s brightness decreases with the ring-opening angle, and it is not visible in either the HST nor the model profiles for 18:30 and 20:00 UT.

As can be observed in the diagram of the rings, before RPX, the Cassini Division is obscured by the F ring on the east ansa. (Note that, whereas the F ring in the photometric model is 60 km in total height, the F ring in the diagram is depicted with a height of only 10 km so that the main rings can be more plainly seen. This narrow band also serves to indicate the position of the densest part of the model F ring.) In the model profiles, the Cassini Division is barely discernible on the west ansa with a $VIF \sim 0.1$ km near 120,000 km, and there is almost no trace of it on the east ansa where the F ring blocks most of the light from the Cassini Division. In most of the HST dark-side profiles there seems to be a small feature with an amplitude

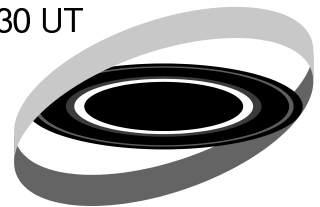
Figure 8: Model profiles of $VIF(r)$ and corresponding diagrams of the ring geometry for each of the HST observations. The F ring is depicted in the diagram as a 10 km-high “ribbon,” but its full height in the photometric model is 60 km. The total brightness, the sum of the other components shown, is plotted as a solid gray line. The dash-dot line shows the brightness of the main rings (MR). A dashed line gives the brightness of the back of the F ring, with light blocked by the main rings removed (BF). The dotted line is the sunlight reflected from the front of the F ring (FF). The solid black line shows the blocking by the front of the F ring of the main rings and the back of the F ring (FBF+FBM), and has negative values. The profiles were created with our best-fitting F-ring model parameters, $h_o=8$ km and $D=10$ km. Note the change in the scale of the y axis in the last three panels.



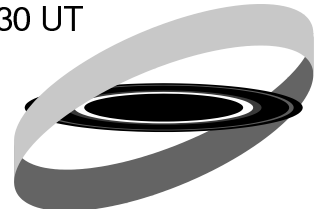
14:00 UT



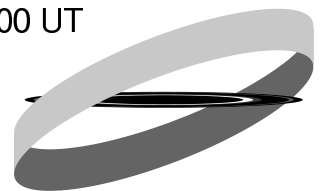
15:30 UT



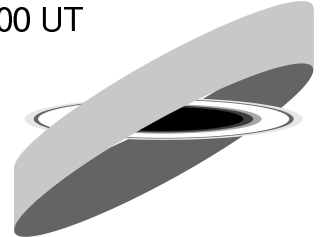
18:30 UT



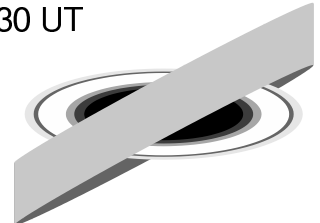
20:00 UT



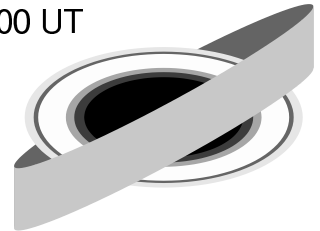
22:00 UT



23:30 UT



25:00 UT



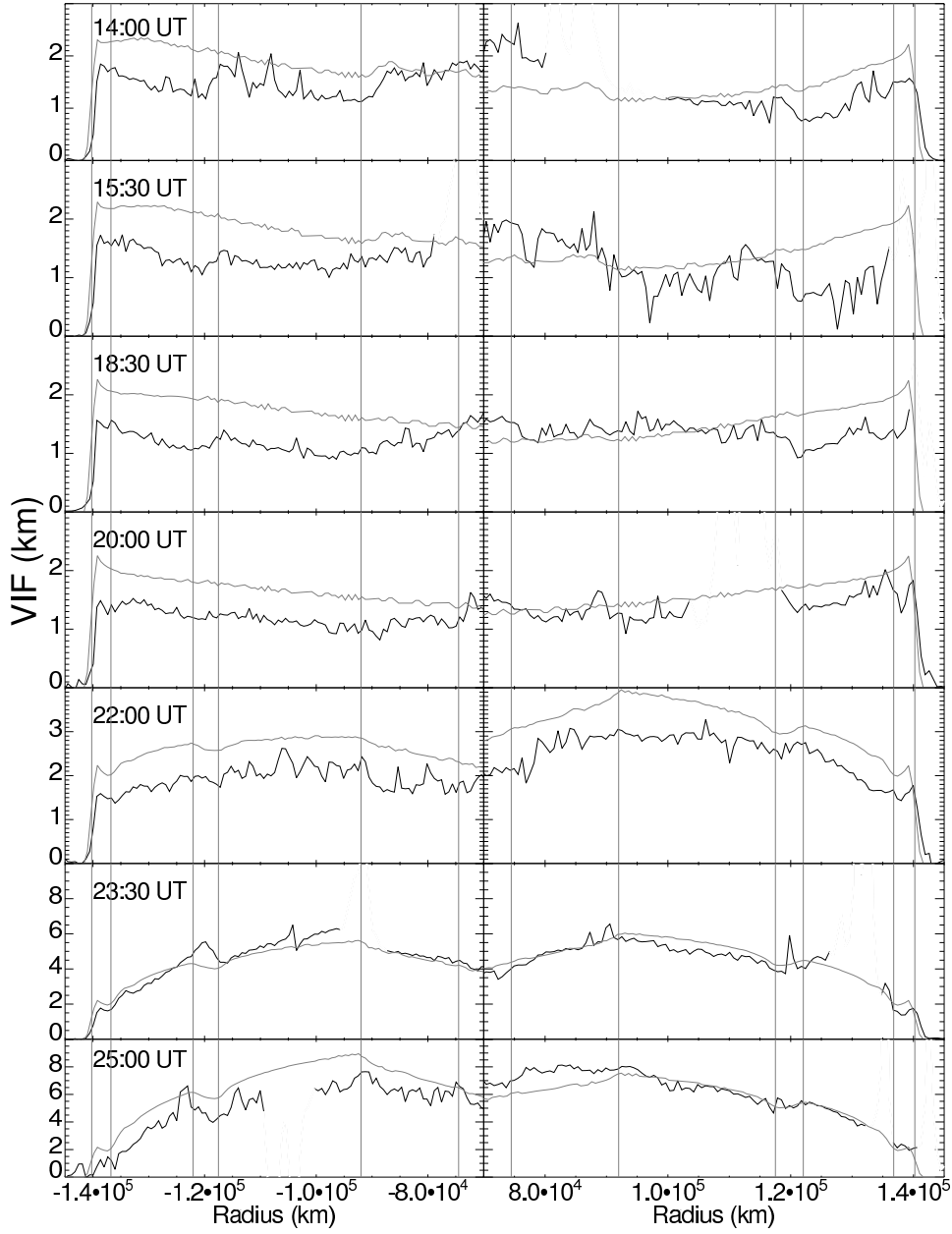


Figure 9: Profiles of $VIF(r)$ from the HST data (black line) and from the model (gray line) for the best-fit parameters $D=10$ km, $h_o=8$ km. The vertical lines indicate the boundaries of the different ring regions as in Fig. 1. Unlike Fig. 1, in this figure we have removed the regions in the HST profiles that are contaminated by light from satellites.

of ~ 0.3 km at the radius of the Cassini Division. It is more prominent on the west ansa. However, the level of noise in the HST profiles makes a positive identification of this feature uncertain.

There are several localized features in the HST dark-side profiles which are not accounted for by the model. Many of these features are present in all the HST profiles that were combined to produce the composite profiles and are not due to an anomaly in a single image. (See, e.g., the two bright features of 0.5 km just inside the Cassini Division and in the C ring in the east ansa profile at 14:00 UT in Fig. 9.) They are also not due to satellites, which have been largely removed by median-filtering. (Portions of the profiles where satellites were not removed effectively have been blanked out in Fig. 9.) Most of these features are probably a result of azimuthal structure (e.g., clumpiness) in the F ring, which is not included in our model. We have found it difficult to track these features with the orbital motion of the F ring in this dataset due to the $\gtrsim 1$ hr gap between visits and the known moons of Saturn that frequently obscure key regions of the profiles, and so are unable to confirm that they are part of the F ring.

5.2.2. Lit-side profiles

The asymmetry in the model brightness after the RPX results arises almost entirely from the differences in the blocking of the sunlit side of the main rings by the front of the F ring.

At 22:00 UT, just ~ 1 hour after the main-ring-plane crossing, our component profiles show that sunlight reflected from the main rings is already comparable in brightness to that reflected from the F ring, and as B_e increases further, so does the VIF; by 23:30 UT the light from the main rings dominates the system's brightness (Fig. 8). Notice that the F ring's brightness is almost independent of the ring-opening angle.

At 22:00 UT, the west ansa is brighter than the east ansa in model profiles, because the dense central region of the F-ring model lies directly in front of the east ansa but falls north of the west ansa (see Fig. 8). The observed asymmetry and the shape of the HST profiles at this time are reproduced well by the model. The maximum in VIF at the inner boundary of the B ring, a slight dip at the Cassini Division, and the small peak at the radius of the F ring on both ansae are seen in both HST and model profiles. The east ansa profile is flatter than the west ansa because of the blocking of the B-ring region at this time (see Fig. 8). The HST profiles are ~ 0.5 km lower than the predicted values at this time but this is mostly because the bulk of the HST images were taken a few minutes before 22:00 UT, the time chosen to represent this HST visit in the model, and the main rings are opening rapidly (see Fig. 2).

At 23:30 UT, near the F-ring-plane crossing, the model F ring obscures both ansae to a similar extent, leading to little if any asymmetry in ring brightness. The shape of the model profiles is also quite a good match to the HST profiles.

At 25:00 UT, the F ring still partially blocks the east ansa, but blocks much more of the west ansa. Considering the noisiness of the HST east ansa profile, which is made from the mean of only two profiles and contaminated by a bright satellite, the agreement in the general shape of the profile is fair. It is very good on the west ansa, except in the inner C ring, where the HST VIF is ~ 1 km greater than the model. We suspect that this is a clump in the F ring itself, but due to the noise in the HST profiles and the presence of contaminating satellites, we were unable to definitively identify this feature at any other times, and thus we cannot confirm that it is an F-ring feature.

5.3. $\langle VIF \rangle$ vs. t

While the comparison of the model and HST profiles of $VIF(r)$ discussed in Sec 5.2 demonstrates that the model reproduces the HST data in a qualitative way, our model is actually constrained by the brightness asymmetry between ansae in the HST observations. Fig. 10 shows the $\langle VIF \rangle$ of our best-fitting model along with the $\langle VIF \rangle$ measured from each ansa of the WF3 HST images.

Before the ring-plane crossing, the average model brightness of all dark-side points (including the east and west ansae) matches the average HST brightness because this is how we scaled the albedo of the model F ring. As discussed in Sec. 5.2.1, it is clear that the asymmetries in the model do not match the asymmetries in the HST data on the dark side.

On the lit side, however, the model provides a good match to the HST data. At 22:00 UT, the west ansa is brighter than the east ansa in both the model and the data and by about the same amount. At 23:30 UT,

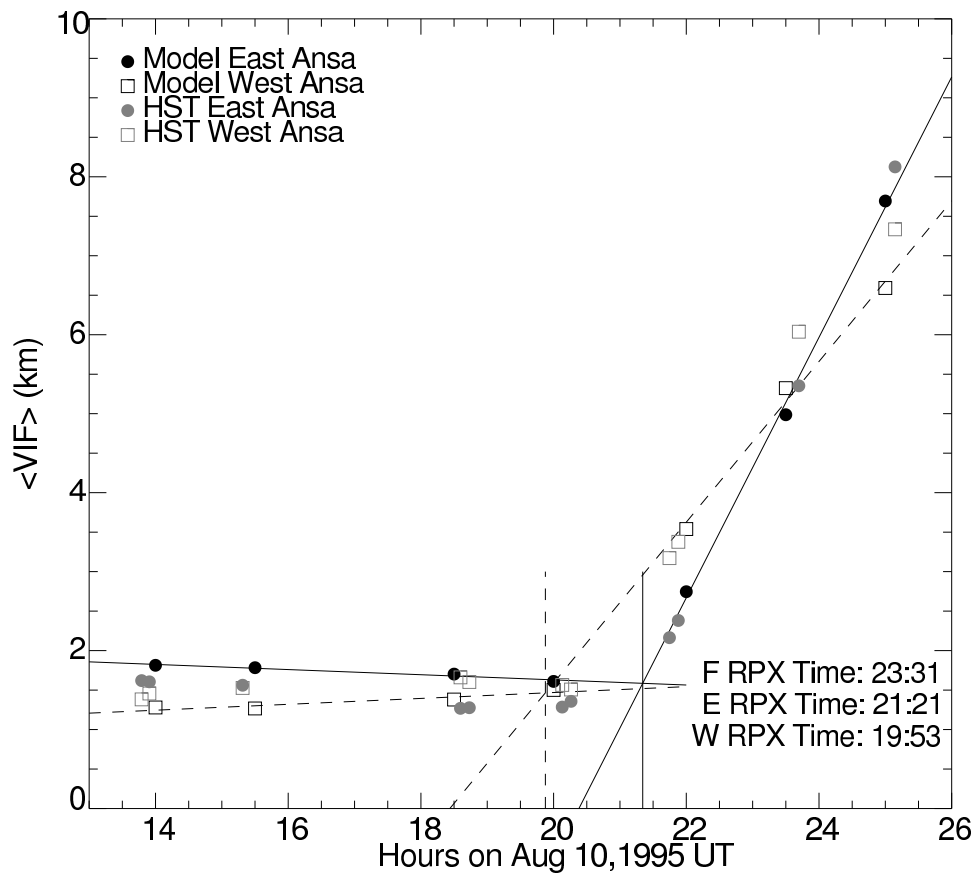


Figure 10: $\langle VIF \rangle$ as a function of time, showing the model results (black) and the HST WF3 data (gray). The intersections of separate linear fits to the model brightness before and after the RPX are used to calculate a RPX time for each ansa. The intersection of the east and west ansa fits on the lit side gives the FRPX time.

the west ansa is still brighter, but the amplitude of the asymmetry has greatly decreased. By 25:00 UT, the east ansa is brighter than the west ansa, and the asymmetry is large once again.

To compare to Nicholson et al. (1996), we do a linear fit to the model predictions for each ansa, fitting the points before and after the RPX separately. The intersection of these fits gives a model RPX time for each ansa. We find a ring-plane-crossing time of 19:53 UT for the west ansa and 21:21 UT for the east ansa. As discussed previously, from the WF3 HST data, we find a west-ansa crossing time of $20:25 \pm 10$ min and an east-ansa crossing time of $21:13 \pm 3$ min. The model RPX time on the west ansa differs significantly from the HST time, in part due to the failure of the model to reproduce the change in brightness with time of the rings before the ring-plane crossing, and in part due to the low slope of the fit to the lit-side west-ansa model VIFs.

We can also compute the intersection of the east and west ansa *lit-side* linear fits to find the time for the F-ring-plane crossing (FRPX). This result is more robust, because it does not involve the dark-side model prediction, and, because it depends on the orientation of the F ring, allows us to assess the F-ring orbital model that was used to create our photometric model. From the HST data, if we fit both PC and WF3 data, as in Fig. 2, the FRPX time is 23:24 UT. Using just the WF3 data as in Fig. 3, we compute an FRPX time of 24:09 UT (which is actually 00:09 UT on 11 August). We take the difference of 45 min as an indication of the experimental uncertainty in the FRPX time.

In the model results, the time of the F-ring-plane crossing shows little dependence on the choice of photometric parameters of the F ring. It does depend on the orientation of the F-ring plane, which is determined by the inclination and the ascending node. To find the sensitivity of the model results to small changes in the orbital elements of the F ring, we made several models with values for the inclination and the longitude of the ascending node increased and decreased by the standard errors given by Bosh et al. (2002). All these runs were conducted with $h_o = 10$ km and $D=5$ km.

For nominal values of the inclination and the longitude of the ascending node ($i = 0.0064^\circ$ and $\Omega_o = 17.3^\circ$) for this model, we find a predicted FRPX time of 23:29 UT. Increasing the longitude of the ascending node, which moves the node to the west on the sky, causes an earlier FRPX. For the nominal inclination and $\Omega_o = 13.4^\circ$, the FRPX time is 24:06 UT on 10 August 1995, and for $\Omega_o = 21.2^\circ$ the FRPX time is 23:21 UT. Increasing the inclination of the F ring has the effect of delaying the FRPX time. With the nominal value for the longitude of the ascending node at epoch and an inclination $i = 0.0057^\circ$, the FRPX time was computed to be 23:20 UT, and for $i = 0.0071^\circ$, the FRPX time was 24:09 UT.

Thus, varying the inclination and longitude of the node within the quoted errors of the Bosh et al. (2002) orbit can change the time of the FRPX calculated from model results by ± 25 min, which is comparable to the uncertainty in the FRPX time that is measured from linear fits to the HST data. Because the F-ring blocking affects the model brightness before and after RPX, varying i and Ω_o also affects the model asymmetries and changes the main ring crossing times. However, this change is less than 2 min. The changes in the asymmetries resulted in changes in χ^2 of up to 17%, much less than the $1-\sigma$ level of expected statistical variation.

Based on this experiment, we are confident in using the best-fit F-ring orbit of Bosh et al. (2002) to determine the geometry for our model. Our model results show that a change in i or Ω_o much greater than the stated $1-\sigma$ uncertainties would lead to a significantly poorer fit to the HST data, but we do not have enough sensitivity to the node or inclination in these data to improve on the fit of Bosh et al. (2002).

6. Conclusions

Our photometric model demonstrates that the inclination of the F ring provides a plausible explanation for the asymmetry in brightness between the east and west ansae of the rings of Saturn within a few hours after the Earth ring-plane crossing of 10 August 1995, as originally suggested by Nicholson et al. (1999).

6.1. Profiles of Brightness vs. Distance

Despite its simplicity, the model also does a fair job of reproducing the general shape of the HST profiles. Both observed and model profiles of the dark side of the rings are flat, with a slight increase in brightness

at the ansa. The shape of the lit-side model profiles are a particularly good match to the HST data. They show the observed features of the main ring profile clearly, including a small brightening at the location of the Cassini Division, and show how the brightness of the main rings increases with the ring-opening angle. The model profiles also show how blocking of the main rings by the front of the F ring flattens the shape of the HST profiles.

6.2. Equivalent Depth

The best-fit equivalent depth of this model, $D=10\pm 4$ km, is in agreement with the equivalent depth of 8 ± 3 km of Poulet et al. (2000), but both of these are larger than the equivalent depths derived from profiles of optical depth of the F ring obtained from occultations observed from Voyager and from Earth in the 1980s. However, as shown in Table. 4, the equivalent depth of that we measure for the F ring may fit into a trend of increasing equivalent depth observed between the Voyager and Cassini epochs.

There are also other hints that the F ring's behavior is also not uniform over decadal timescales. Averaging the equivalent depths reported for 87 Cassini VIMS stellar occultations yields a mean equivalent depth of 6 ± 3 km at $3.2 \mu\text{m}$ (Hedman et al., 2011), which agrees with the results the present model and Poulet et al. (2000). Stellar occultations observed with Cassini UVIS yield equivalent depths between 4 and an extreme upper limit of 51 km at different longitudes (Albers et al., 2012). By comparing the brightness of the F ring in Cassini and Voyager images, and optical depth profiles from occultations from both missions, French et al. (2012) found that the brightness and equivalent depth of the F ring has increased by a factor of 2–3, since the Voyager epoch.

It is likely that this change is due to small particles being freed from the surface of larger parent bodies due to collisions or gravitational interactions between objects inside and near the F ring, but the exact mechanism is unknown. French et al. (2012) reject close encounters between Prometheus and the core at Prometheus' apoapse as the sole cause of the brightening, because Prometheus' distance from the F-ring core has varied significantly during the Cassini mission, will the F ring's brightness has stayed fairly constant.

6.3. Azimuthal Variation

The mechanism which produces an asymmetry in ring brightness on the dark side of the rings in our model, i.e. blocking of the back of the F ring by the main ring, does not account for the asymmetry in the brightness observed in the HST images prior to RPX. Instead this is probably due to the significant longitudinal variations exhibited by the F ring.

It is well-known that the characteristics of the F ring are not uniform longitudinally due to complex dynamical interactions with Prometheus (Kolvoord et al., 1990; Murray et al., 2008) and collisions with smaller moonlets (Kolvoord et al., 1990; Beurle et al., 2010), and Showalter et al. (2009) suggested activity related to clumps can affect the F ring's appearance on short timescales. Cassini occultations at a variety of longitudes distributed around the F ring find a range of equivalent depths measured at different longitudes demonstrates that the azimuthal variability of the F ring is more than enough to cause the small but noticeable asymmetry observed in the HST data before the RPX (French et al., 2012; Albers et al., 2012).

Future photometric models of the F ring can take advantage of far denser coverage in time and longitude from the Cassini spacecraft, and may be able to address the variation in the F ring to create a more complete picture of its azimuthal structure. As the 1995 Earth RPX was used to probe the F ring's vertical structure, ring-plane crossings by Cassini and the 2009 solar ring-plane crossing observed by Cassini have similar potential to improve our understanding of the vertical extent and shape of the F ring even as it varies in longitude and in time. In future publications, we hope to apply our model to Cassini VIMS RPX observations.

Appendix A. A detailed description of the photometric model

This appendix describes the computer model which was used to simulate the brightness of the ring system during the 1995 August ring-plane crossing.

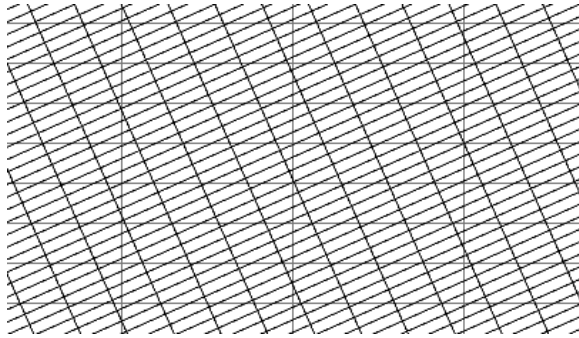


Figure A.11: The relative size and orientation of the main ring pixels and F-ring cells. The main ring pixels (horizontal grid) are $\sigma_u=600$ km wide by $\sigma_v=0.0325$ km high. The F-ring cells are 146.6 km wide by 0.01 km tall, and are tilted due to the inclination of the F ring. This picture shows a region of the u-v plane ~ 2000 km wide by ~ 0.3 km tall, and the vertical scale in this diagram is exaggerated by a factor of 400. A full u-v image is 300,000 km by 130 km.

The ring model is constructed from arrays of pixels, in the case of the main rings, or “cells,” in the case of the F ring. For each pixel or cell, we assign an optical depth, τ , a single-scattering albedo, ϖ_o , a phase factor $P(\alpha)$ and coordinates in space and on the sky. The F ring is separated into a front portion and a back portion. We then create component image layers by computing the transmitted and/or reflected sunlight for each part of the ring model, as well as the transmission of light from the model rings that lie behind, as appropriate. We construct profiles of VIF vs. radius from Saturn’s center for each component, and then sum the profiles to produce the final model profile.

Appendix A.1. Image layers and model resolution

Each image is an array 500×4000 pixels in size. Each pixel is assigned u and v coordinates, with $(0,0)$ being the center of Saturn. The \hat{u} axis points westward along the intersection of the equatorial plane of Saturn and the sky plane, and the \hat{v} axis points along the north pole of Saturn projected onto the sky. The value of each pixel in an image layer is the area-integrated I/F (AIF) for that position on the sky.

We do not vary the model resolution for the different model times; the pixel and cell sizes were chosen so as to be appropriate for both large and small ring-opening angles. The horizontal size of the u-v image is 300,000 km, or 500 pixels, large enough to accommodate the rings’ full diameter with a horizontal pixel size of $\sigma_u = 600$ km, comparable to the HST resolution of ~ 650 km.

We require sufficient vertical resolution to model the F ring’s obscuration of major main-ring features. The narrowest important ring feature, the Cassini Division, has a width of $\Delta a=4537$ km. Its projected height on the sky is smallest at the limb of Saturn, where it is 0.07 km for the smallest $|B_e|$ used in our model, at 20:00 UT. We therefore chose $\sigma_v = 0.0325$ km/pix, and 4000 pixels are required in order to accommodate the extent of the F-ring model at the largest ring-opening angle for the HST dataset, when it has a total height of 130 km on the sky.

We chose the horizontal size of the F-ring cells to be approximately $\frac{1}{4}$ the size of the main-ring pixels. This results in 6000 cells azimuthally around the F ring with a horizontal size of $2\pi a_f/6000=146.6$ km/cell. We chose 6000 cells in the vertical direction, since 6000×6000 was the largest array size for which the modeling computer had sufficient memory. This gives us a vertical cell size of 0.01 km, or about $\frac{1}{3}\sigma_v$.

Fig. A.11 shows the relative sizes and orientations of the main-ring pixels and the F-ring cells as they appear in the model.

The five image layers that make up the model are:

1. The sunlight reflected from the back of the F ring minus that which is blocked by the main rings (henceforth labeled BF).
2. The sunlight reflected or transmitted by the main rings (MR).
3. The light from the back of the F ring that is blocked by the front of the F ring (FBF).

4. The light from the main rings that is blocked by the front of the F ring (FBM).
5. The sunlight reflected from the front of the F ring (FF).

We compute the AIF of each pixel in each layer. The AIF values of the pixels of the blocked-light images (FBF and FBM) are negative, indicating light that is absorbed or scattered by the F ring so that it does not reach the observer.

Theoretically, a total model image could be constructed by summing the image layers. However, because the rings are not vertically resolved in the HST images, there is no reason to produce a final image of the model. Instead, as each layer is computed, a profile of vertically-integrated I/F is extracted, and once it is no longer needed, the image is deleted to free up memory. The VIF profile is given by:

$$\text{VIF}(u) = \frac{1}{\sigma_u} \sum_v \text{I/F}_{\text{pix}}(u, v) \cdot A_{\text{pix}} \quad (\text{A.1})$$

$$= \frac{1}{\sigma_u} \sum_v \text{AIF}_{\text{pix}}(u, v) \quad (\text{A.2})$$

$$= \sigma_v \sum_v \text{I/F}_{\text{pix}}(u, v), \quad (\text{A.3})$$

where $\text{I/F}_{\text{pix}}(u, v)$ is the reflectance computed for the pixel at coordinates (u, v) in the image, and $A_{\text{pix}} = \sigma_u \sigma_v$ is the projected area of the pixel on the sky. The u coordinate is equivalent to r , the horizontal distance from the center of Saturn, measured in the plane of the sky, giving us a profile, $\text{VIF}(r)$. A profile representing the total light scattered from the rings is obtained by summing the profiles of the components, some of which are negative. This is referred to as the total profile, $\text{VIF}_{\text{tot}}(r)$.

The total VIF profile can then be integrated radially to compute the radially averaged, vertically-integrated I/F:

$$\langle \text{VIF} \rangle = \frac{1}{120,000 - 80,000 \text{ km}} \int_{80,000 \text{ km}}^{120,000 \text{ km}} \text{VIF} \cdot dr \quad (\text{A.4})$$

$$= \frac{\sigma_u}{40,000 \text{ km}} \sum_u \text{VIF}(u). \quad (\text{A.5})$$

We average over the same range that was used to compute $\langle \text{VIF} \rangle$ by Nicholson et al. (1996). Just as the total model profile is the sum of the component profiles, the total $\langle \text{VIF} \rangle$ of the ring system is then the sum of the $\langle \text{VIF} \rangle$ s of the components.

Appendix A.2. The Main Ring Model

The reflectance of the main rings in transmitted sunlight (before the RPX) or reflected sunlight (after the RPX) is computed using the single-scattering functions of Chandrasekhar (1960) for a uniform plane-parallel medium. When the Earth is on the dark side of the rings, we use the formula for transmitted light,

$$\text{I/F} = \frac{1}{4} P(\alpha) \varpi_o \frac{\mu_o}{\mu - \mu_o} \left(e^{-\tau/\mu} - e^{-\tau/\mu_o} \right). \quad (\text{A.6})$$

and when the Earth is on the lit side of the rings, we use the formula for reflected light,

$$\text{I/F} = \frac{1}{4} P(\alpha) \varpi_o \frac{\mu_o}{\mu + \mu_o} \left(1 - e^{-\tau(1/\mu + 1/\mu_o)} \right), \quad (\text{A.7})$$

In these expressions, $\mu = \sin |B_e|$ and $\mu_o = \sin |B_s|$, where B_e and B_s are listed in Table 1.

The area-integrated I/F of the pixel is then:

$$\text{AIF} = \text{I/F}_{\text{pix}} \sigma_u \sigma_v. \quad (\text{A.8})$$

The center of the planet is located at the center of the image. Using u-v coordinates, the distance of each pixel from the planet’s center in the ring plane is computed: $R = \sqrt{u^2 + (v/\sin B_e)^2}$. An albedo is assigned to each pixel of the main-ring array based on its radius, R , using the values in Table 6.

Optical depths are assigned in a similar way, based on the Lick optical depth profile shown in Fig. A.12. The majority of the transmitted light in the model passes through the Cassini Division and the C Ring (as seen in Fig. 8). According to Eq. A.6, the transmitted reflectance peaks strongly when $\mu < \tau < \mu_o$, and since at ring-plane crossing μ is very small, the computed reflectance is very sensitive to optical depths near zero, so we must be cautious about the portions of the profile where the optical depth is very small. Typical noise levels in the Lick observations of the flux of the occulted star were $\sigma(F_{obs})/F_o=0.025$, where F_{obs} was the observed flux of the occulted star and F_o its unocculted flux. The computed optical depth is

$$\tau = -\mu \ln \left(\frac{F_{obs}}{F_o} \right), \quad (\text{A.9})$$

where $\mu = \sin B_e = 0.429$. (Nicholson et al., 2000). Thus the 2.5% noise level results in an uncertainty in τ of 0.01. Whenever the optical depth value is less than this, it is set to zero to eliminate spurious peaks in the computed reflectance profiles.

In the Voyager observations, which span phase angles of 6°–155°, the rings obey a power-law phase function which is suitable for macroscopic particles:

$$P(\alpha) = c_n(\pi - \alpha)^n, \quad (\text{A.10})$$

where c_n is a normalization constant. The phase function of the A ring is similar to the phase function of Callisto, with $n = 3.301$ and $c_n = 0.130$. (Dones et al., 1993)

This is the phase function we adopt for the main rings, despite the low phase angle of the HST observations.

We interpolate the ring opening angles to the Sun and Earth from ephemerides from the Planetary Data System’s Rings Node (<http://pds-rings.seti.org>) using the nominal time for each HST visit in Table 1.

Appendix A.3. The F-ring model

The F ring of our model is constructed as an inclined “ribbon” of cells that are smaller than the main ring pixels. Each cell’s radial optical depth is determined using a Gaussian profile with height given by Eq. 10. The F ring is divided into a front half and back half. We create positive-valued 2-D images of the sunlight reflected from the front (FF) and back (FB), and negative-valued images of light absorbed or scattered by the F ring from the back of the F ring (FBF) and the main rings (FBM).

Appendix A.3.1. Constructing the F-ring model

To determine the geometry of the F ring at the time of these observations, we must take into account the regression of the F ring’s ascending node. Its longitude is measured from the ascending node of Saturn’s equatorial plane on the Earth’s equatorial plane of J2000.0. The orientation of Saturn’s equatorial plane is derived from the position of its pole, which was not available from the Rings Node ephemeris, so we compute the right ascension and declination of Saturn’s pole (α_p, δ_p) using the pole and precession rate of Saturn derived by French et al. (1993). Combined with Saturn’s right ascension and declination, this allows us to find the position of the ascending node (on the Earth’s equatorial plane) of Saturn’s equatorial plane relative to the line of sight to the observer, to which we can refer the ascending node of the F ring.

The F ring model is created as a collection of two-dimensional arrays. There are $m_f = 6000$ cells in the azimuthal direction and, coincidentally, $n_f = 6000$ cells in the vertical direction. Each cell is assigned an azimuthal coordinate θ_f , relative to the line of sight to the observer projected into the F-ring plane, and a vertical coordinate h . The distance from Saturn is taken as a constant, equal to the semimajor axis, a_f . Each cell is also assigned a radial optical depth τ_r based on its h value.

Once the arrays have been constructed, the cells can be positioned in space by transforming their coordinates. Using the F ring’s inclination and the orientation of its ascending node, the array containing

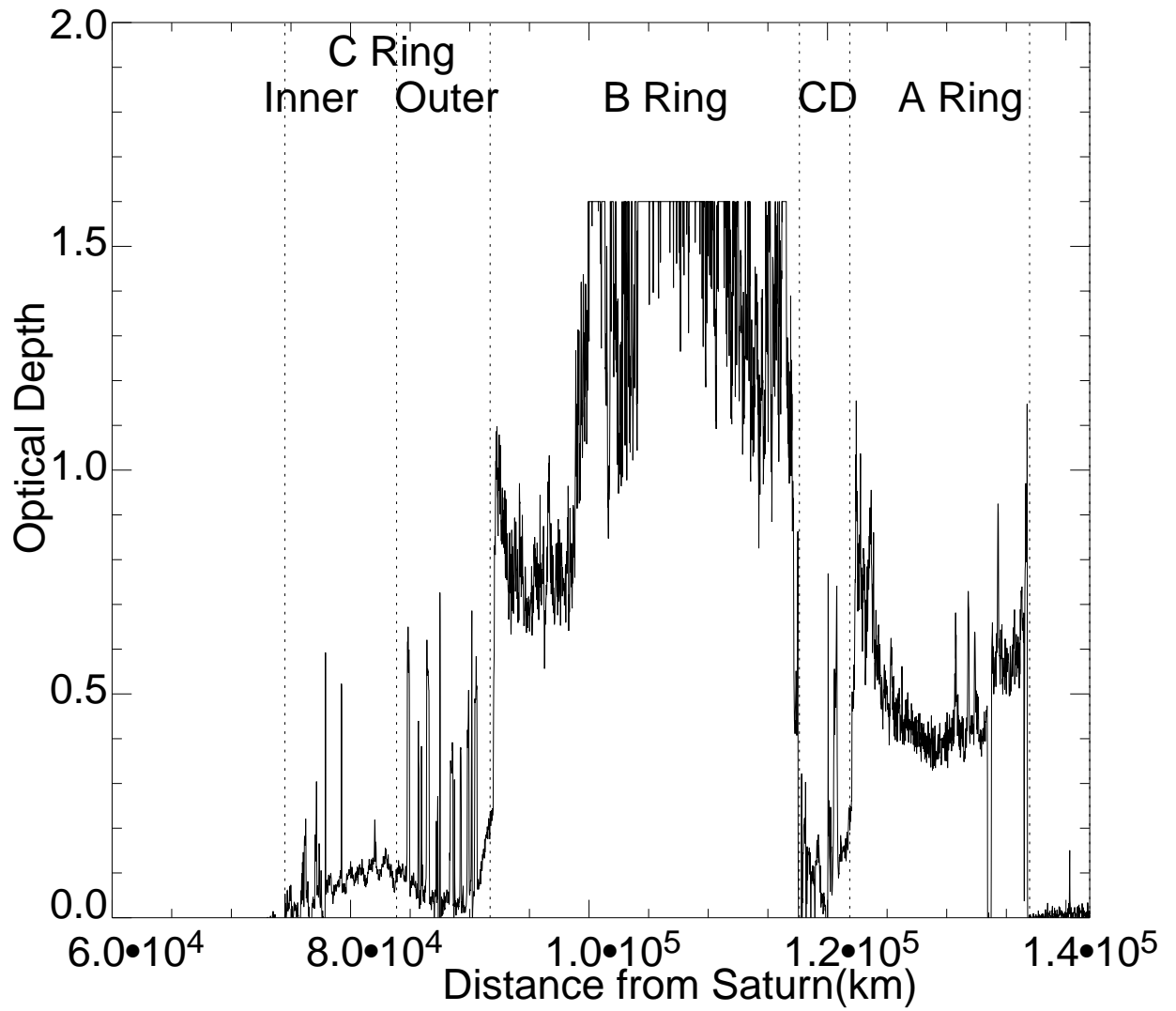


Figure A.12: The profile of optical depths used for the main-ring model, taken from an observation of the occultation of the star 28 Sgr by the rings (Nicholson et al., 2000). This plot is cut off at $\tau = 1.6$, which is the maximum detectable optical depth in the Lick egress data. The affected regions in the B ring are all optically thick, so the exact value of τ is not important for calculating the I/F near RPX.

cylindrical F-ring coordinates, (r_f, θ_f, h) for each cell, can be transformed by matrix rotation to Saturn equatorial coordinates and then to sky-plane coordinates. The origin of the coordinate systems is the center of Saturn. The \hat{x} axis of Saturn equatorial coordinates is the projection of a vector toward Earth into Saturn's equatorial plane, the \hat{y} axis points westward in Saturn's equatorial plane and the plane of the sky, and \hat{z} is aligned with Saturn's north pole. For the sky-plane coordinates, $\hat{u} = \hat{y}$, and \hat{v} is aligned with the projection of \hat{z} into the sky plane.

We split the F ring into the back and front halves by making separate lists of cells with $x < 0$ and $x > 0$ respectively.

The product of the albedo and phase function of the F ring are initially set to $P(\alpha)\varpi_o = 1$. The F-ring brightness and will be scaled later to match the observed dark-side brightness of the rings.

The main rings are treated as thin and flat so that $\mu = \sin |B_e|$ for all points on the ring, but the F ring is modeled as a vertical surface, so that

$$\mu \sim \mu_o = \cos(\theta_f) \quad (\text{A.11})$$

where θ_f is measured in Saturn equatorial coordinates from the sub-Earth point on the F ring. Thus the I/F of each F-ring cell due to reflected sunlight is computed using Eq. A.7:

$$\text{I/F} = \frac{1}{8} P(\alpha)\varpi_o \left(1 - e^{-2\tau_r(h)/\mu(\theta)} \right). \quad (\text{A.12})$$

Multiplying by the projected area of the cell, $dh = \frac{h_f}{n_f} \frac{2\pi r_f}{m_f} |\mu|$, yields the AIF of each cell. (We must take the absolute value of the cosine because the θ values for the back of the F ring are between $\pi/2$ and $3\pi/2$.)

To create an image of the F ring's brightness, we first create a standard 500×4000 -pixel image array with a value of zero for all pixels. The AIF of the reflected sunlight of each cell in the front of the F ring is then added to the appropriate pixel, creating the FF image.

The same process is used to create an image of the sunlight reflected from the back half of the F ring, BF, except that the I/F of the pixels where the back of the F ring lies behind the main rings is set to zero. (The main ring opening angle is very small, and even in the C ring and Cassini Division, $\tau/\mu \sim 0.02/0.008 = 2.5$. Therefore light reflected from the back half of the F ring and transmitted through the main rings is negligible.)

We also create two image layers to represent the light blocked by the front of the F ring: the blocked light from the back of the F ring (FBF) and the blocked light from the main rings (FBM). For each of these, we create an image array with all the pixel values set to zero. Because F-ring cells are smaller than u-v pixels, we simply use the (u, v) coordinate of the center of each F-ring cell to determine what pixel of the blocked image is behind the cell. Then the I/F of that pixel is multiplied by the factor $1 - e^{-\tau_r/\mu}$ to find the I/F_b that is blocked by the cell. This is multiplied by the projected area of the F-ring cell to find the AIF_b absorbed or scattered by the cell. The AIF_b blocked by each cell in the front of the F ring is then *subtracted* from the pixel upon which the center of the cell falls. This process is performed on the BF layer and the MR layer, creating the negative-valued FBF and FBM layers, respectively.

Appendix A.3.2. Albedo scaling

To begin a complete model run, each of the image layers is computed for the four dark-side observation times (14:00–20:00 UT). During these times, the brightness contributed by the main ring is much less than the brightness contributed by the F ring, so the profile of the total ring brightness is approximately

$$\text{VIF}_{tot}(r) \approx \text{VIF}_{BF}(r) + \text{VIF}_{FBF}(r) + \text{VIF}_{FF}(r), \quad (\text{A.13})$$

and also

$$\langle \text{VIF} \rangle_{tot} \approx \langle \text{VIF} \rangle_{BF} + \langle \text{VIF} \rangle_{FBF} + \langle \text{VIF} \rangle_{FF}. \quad (\text{A.14})$$

Initially, we set $P(\alpha)\varpi_o = 1$. This provisional model brightness at each time is then represented by VIF' . The same factor $P(\alpha)\varpi_o$ is present in the single-scattering equations used to compute the I/F of sunlight reflected by the front and the back of the F ring. When the FBF layer is computed, the reflected light from

the back of the F ring is simply reduced by the factor $e^{-\tau_r/\mu}$, so the FBF layer depends linearly on $P(\alpha)\varpi_o$ as well. The model values therefore can be rescaled by a factor p_f representing the factor $P(\alpha)\varpi_o$, so that

$$p_f = \langle \text{VIF} \rangle_{HST} / \langle \text{VIF}' \rangle_{tot}, \quad (\text{A.15})$$

where $\langle \text{VIF} \rangle_{HST}$ is the radially-averaged, vertically-integrated I/F measured for this time from the HST observations.

We use the $\langle \text{VIF} \rangle_{HST}$ values from Table 3 to compute p_f for each ansa at each time before the RPX, then average them all together. Each $\text{VIF}'_{BF}(r)$, $\text{VIF}'_{FBF}(r)$, and $\text{VIF}'_{FF}(r)$ is multiplied by this average p_f to obtain the final model profiles $\text{VIF}_{BF}(r)$, $\text{VIF}_{FBF}(r)$, and $\text{VIF}_{FF}(r)$.

The brightness of the lit side of the rings includes significant contributions from both the F ring and the main rings. We have determined an empirical value of $p_f = P(\alpha)\varpi_o$, which can now be used in computations of the I/F of the F ring on the lit side, but for the main rings, the albedo remains uncertain. We use the nominal values of $P(\alpha)\varpi_o$ described in Sec. 4.3 to compute $\text{VIF}'(r)$ for the main rings, but these must also be corrected by some factor p_m . The total model brightness on the lit side of the rings can be expressed as:

$$\text{VIF}_{tot}(r) = \text{VIF}_{BF}(r) + p_m \text{VIF}'_{MR}(r) + \text{VIF}_{FBF}(r) + p_m \text{VIF}'_{FBM}(r) + \text{VIF}_{FF}(r). \quad (\text{A.16})$$

On the lit side again, we want the average model brightness to match the HST brightness, so we set $\langle \text{VIF} \rangle_{tot} = \langle \text{VIF} \rangle_{HST}$ for each ansa at each time, and solve Eq. A.16 for:

$$p_m = \frac{\langle \text{VIF} \rangle_{HST} - (\langle \text{VIF} \rangle_{BF} + \langle \text{VIF} \rangle_{FBF} + \langle \text{VIF} \rangle_{FF})}{\langle \text{VIF}' \rangle_{MR} + \langle \text{VIF}' \rangle_{FBM}}. \quad (\text{A.17})$$

This factor, averaged over all the lit-side data points, is then applied to all computed profiles $\text{VIF}'_{MR}(r)$ and $\text{VIF}'_{FBM}(r)$, including those for the dark-side.

We can then finally find $\text{VIF}_{tot}(r)$ using Eq. A.16. This profile, and its average over the range $r = 80,000$ – $120,000$ km, represent the output of the model, which we then compare to the HST data.

The results of the model were verified for simple test cases, e.g. matching the HST ring brightness profile of Nicholson et al. (1996) from the solar ring-plane crossing of 21 November 1995, when, due to the larger Earth ring-opening angle, the F ring does not obscure the main rings. The model brightness profile is shown in Fig. A.13, for comparison with Fig. 4 of Nicholson et al. (1996). At this time, saturnshine was an important source of illumination of the rings, but our model shows that the saturnshine was not a significant component of the ring brightness for the August RPX. The saturnshine computation is explained in Scharringhausen (2007).

References

- Albers, N., Sremčević, M., Colwell, J. E., Esposito, L. W., 2012. Saturn's F ring as seen by Cassini UVIS: Kinematics and statistics. *Icarus* 217, 367–388.
- Barbara, J. M., Esposito, L. W., 2002. Moonlet collisions and the effects of tidally modified accretion in Saturn's F ring. *Icarus* 160, 161–171.
- Beurle, K., Murray, C. D., Williams, G. A., Evans, M. W., Cooper, N. J., Agnor, C. B., 2010. Direct Evidence for Gravitational Instability and Moonlet Formation in Saturn's Rings. *Astrophysical Journal Letters* 718, L176–L180.
- Bobrov, M. S., 1972. Thickness of Saturn's rings from observations in 1966. *Astronomicheskij Zhurnal* 49, 427–435.
- Bosh, A. S., Olkin, C. B., French, R. G., Nicholson, P. D., 2002. Saturn's F ring: Kinematics and particle sizes from stellar occultation studies. *Icarus* 157, 57–75.
- Bosh, A. S., Rivkin, A. S., Percival, J. W., Taylor, M., van Citters, G. W., 1997. NOTE: Saturn ring-plane crossing, May 1995: Pole precession and ring thickness. *Icarus* 129, 555–561.
- Brahic, A., Sicardy, B., 1981. Apparent thickness of Saturn's rings. *Nature* 289, 447–450.
- Chandrasekhar, S., 1960. *Radiative Transfer*. New York : Dover.
- Charnoz, S., Porco, C. C., Déau, E., Brahic, A., Spitale, J. N., Bacques, G., Baillie, K., Nov. 2005. Cassini Discovers a Kinematic Spiral Ring Around Saturn. *Science* 310, 1300–1304.
- Cooke, M. L., 1991. Saturn's Rings: Photometric Studies of the C Ring and Radial Variation in the Keeler Gap. Ph.D. thesis, Cornell University.
- Dollfus, A., 1979. Photometric determination of the Saturn rings' thickness. *Astronomy and Astrophysics* 75, 204–206.
- Dones, L., Cuzzi, J. N., Showalter, M. R., 1993. Voyager photometry of Saturn's A ring. *Icarus* 105, 184–215.

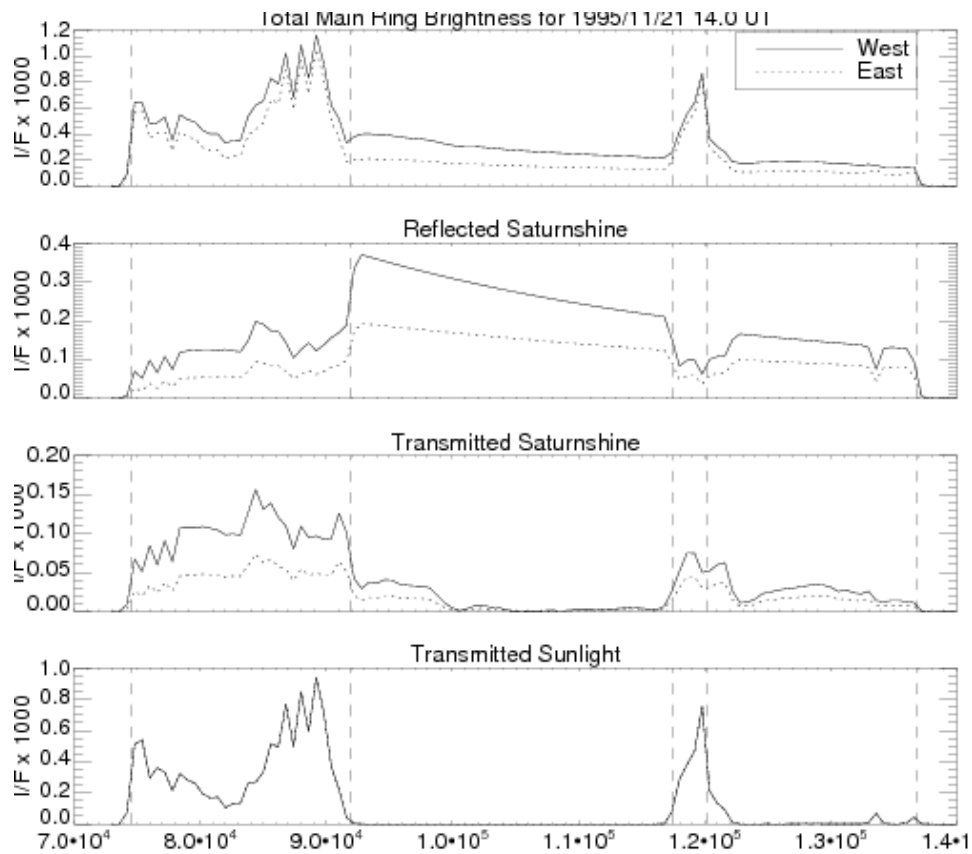


Figure A.13: A model of the brightness of the east and west ansa as a function of distance from the center of Saturn, including saturnshine from the northern hemisphere of the planet reflected from the rings, and saturnshine from the southern side of the planet transmitted through the rings, and sunlight transmitted through the rings. The F ring is not included in this model; the asymmetry between the east and west ansae comes from the fact that at the time of the observation, the phase angle was large and the Sun illuminated the western face of Saturn to a greater degree. This reproduces the main-ring profiles shown in Fig 4 of Nicholson et al. (1996).

- Doyle, L. R., Dones, L., Cuzzi, J. N., 1989. Radiative transfer modeling of Saturn's outer B ring. *Icarus* 80, 104–135.
- Esposito, L. W., Cuzzi, J. N., Holberg, J. B., Marouf, E. A., Tyler, G. L., Porco, C. C., 1984. Saturn's rings—Structure, dynamics, and particle properties. In: Gehrels, T., Matthews, M. (Eds.), *Saturn*. Tucson: University of Arizona Press, pp. 463–545.
- Esposito, L. W., Meinke, B. K., Colwell, J. E., Nicholson, P. D., Hedman, M. M., Mar. 2008. Moonlets and clumps in Saturn's F ring. *Icarus* 194, 278–289.
- Fountain, J. W., Larson, S. M., 1978. Saturn's ring and nearby faint satellites. *Icarus* 36, 92–106.
- French, R. G., Nicholson, P. D., Cooke, M. L., Elliot, J. L., Matthews, K., Perkovic, O., Tollestrup, E., Harvey, P., Chanover, N. J., Clark, M. A., Dunham, E. W., Forrest, W., Harrington, J., Pipher, J., Brahic, A., Grenier, I., Roques, F., Arndt, M., 1993. Geometry of the Saturn system from the 3 July 1989 occultation of 28 SGR and Voyager observations. *Icarus* 103, 163–214.
- French, R. G., Nicholson, P. D., Gordon, M. K., 2003. Radial profiles of Saturn's rings from the Lick 1 Meter Telescope observations of the 1989 occultation of 28 Sgr, LICK1M- SR-CCDC-4-OCC-V1.0, USA_NASA_PDS_EBROCC_0001.
- French, R. S., Showalter, M. R., Sfair, R., Argüelles, C. A., Pajuelo, M., Becerra, P., Hedman, M. M., Nicholson, P. D., 2012. The brightening of Saturn's F ring. *Icarus* 219, 181–193.
- Gehrels, T., Baker, L. R., Beshore, E., Blenman, C., Burke, J. J., Castillo, N. D., Dacosta, B., Degewij, J., Doose, L. R., Fountain, J. W., Gotobed, J., Kenknight, C. E., Kingston, R., McLaughlin, G., McMillan, R., Murphy, R., Smith, P. H., Stoll, C. P., Strickland, R. N., Tomasko, M. G., Wijesinghe, M. P., Coffeen, D. L., Esposito, L. W., 1980. Imaging photopolarimeter on Pioneer Saturn. *Science* 207, 434–439.
- Goldreich, P., Tremaine, S. D., 1978. The velocity dispersion in Saturn's rings. *Icarus* 34, 227–239.
- Hedman, M. M., Nicholson, P. D., Showalter, M. R., Brown, R. H., Buratti, B. J., Clark, R. N., Baines, K., Sotin, C., Oct. 2011. The Christiansen Effect in Saturn's narrow dusty rings and the spectral identification of clumps in the F ring. *Icarus* 215, 695–711.
- Karkoschka, E., 1994. Spectrophotometry of the jovian planets and Titan at 300- to 1000-nm wavelength: The methane spectrum. *Icarus* 111, 174–192.
- Kolvoord, R. A., Burns, J. A., Showalter, M. R., 1990. Periodic features in Saturn's F ring - Evidence for nearby moonlets. *Nature* 345, 695–697.
- Lane, A. L., Hord, C. W., West, R. A., Esposito, L. W., Coffeen, D. L., Sato, M., Simmons, K. E., Pomphrey, R. B., Morris, R. B., 1982. Photopolarimetry from Voyager 2—Preliminary results on Saturn, Titan, and the rings. *Science* 215, 537–543.
- Lissauer, J. J., Shu, F. H., Cuzzi, J. N., 1984. Viscosity in Saturn's rings. In: A. Brahic (Ed.), *Planetary Rings*. Tucson: University of Arizona Press, pp. 385–392.
- Lumme, K., Irvine, W. M., 1979. Low tilt angle photometry and the thickness of Saturn's rings. *Astronomy and Astrophysics* 71, 123–130.
- Marouf, E. A., Tyler, G. L., Rosen, P. A., 1986. Profiling Saturn's rings by radio occultation. *Icarus* 68, 120–166.
- Marouf, E. A., Wong, K., French, R., Rappaport, N., McGhee, C., 2010. The Discontinuous Core of Saturn's F-Ring and Orbit Model. *Bulletin of the American Astronomical Society* 42, 988.
- McGhee, C. A., Nicholson, P. D., French, R. G., Hall, K. J., 2001. HST observations of saturnian satellites during the 1995 ring plane crossings. *Icarus* 152, 282–315.
- Meinke, B. K., Esposito, L. W., Albers, N., Sremcevic, M., 2010. Classification of F Ring Features Observed in Cassini UVIS Occultations. *Bulletin of the American Astronomical Society* 42, 982.
- Murray, C. D., Beurle, K., Cooper, N. J., Evans, M. W., Williams, G. A., Charnoz, S., 2008. The determination of the structure of Saturn's F ring by nearby moonlets. *Nature* 453, 739–744.
- Murray, C. D., Burns, J. A., Beurle, K., Cooper, N., Evans, M. W., Porco, C. C., Dones, L., Brahic, A., Spitale, J., Cassini Imaging, 2004. Cassini ISS observations of Saturn's F ring region. *Bulletin of the American Astronomical Society* 36, 1077.
- Murray, C. D., Chavez, C., Beurle, K., Cooper, N., Evans, M. W., Burns, J. A., Porco, C. C., 2005. How Prometheus creates structure in Saturn's F ring. *Nature* 437, 1326–1329.
- Nicholson, P. D., Cooke, M. L., Pelton, E., 1990. An absolute radius scale for Saturn's rings. *Astronomical Journal* 100, 1339–1362.
- Nicholson, P. D., French, R. G., Bosh, A. S., 1999. The F ring: Saturn's crooked halo? *Bulletin of the American Astronomical Society* 31, 1229.
- Nicholson, P. D., French, R. G., Tollestrup, E., Cuzzi, J. N., Harrington, J., Matthews, K., Perkovic, O., Stover, R. J., 2000. Saturn's rings I. Optical depth profiles from the 28 Sgr occultation. *Icarus* 145, 474–501.
- Nicholson, P. D., Showalter, M. R., Dones, L., French, R. G., Larson, S. M., Lissauer, J. J., McGhee, C. A., Sicardy, B., Seitzer, P., Danielson, G. E., 1996. Observations of Saturn's ring-plane crossing in August and November. *Science* 272, 509–516.
- Olkin, C. B., Bosh, A. S., 1996. The inclination of Saturn's F ring. *Bulletin of the American Astronomical Society* 28, 1125.
- Poulet, F., Sicardy, B., Dumas, C., Jorda, L., Tiphène, D., 2000. The crossings of Saturn ring plane by the Earth in 1995: Ring thickness. *Icarus* 145, 147–165.
- Press, W. H., Teukolsky, S. A., Vetterling, W. T., Flannery, B. P., 1992. *Numerical Recipes in FORTRAN. The Art of Scientific Computing*, 2nd Edition. Cambridge: University Press.
- Salo, H., Karjalainen, R., 2003. Photometric modeling of Saturn's rings I. Monte Carlo method and the effect of nonzero volume filling factor. *Icarus* 164, 428–460.
- Scharringhausen, B. R., 2007. A Photometric Model of the Inclined F Ring of Saturn. Ph.D. thesis, Cornell University.
- Showalter, M. R., 2004. Disentangling Saturn's F ring. I. Clump orbits and lifetimes. *Icarus* 171, 356–371.
- Showalter, M. R., French, R. S., Sfair, R., Argüelles, C., Pajuelo, M., Becerra, P., Hedman, M. M., Nicholson, P. D., 2009. The Brightening of Saturn's F Ring. *Bulletin of the American Astronomical Society* 41, 896.

- Showalter, M. R., Pollack, J. B., Ockert, M. E., Doyle, L. R., Dalton, J. B., 1992. A photometric study of Saturn's F ring. *Icarus* 100, 394–411.
- Sicardy, B., Lecacheux, J., Laques, P., Despiiau, R., Auge, A., 1982. Apparent thickness and scattering properties of Saturn's rings from March 1980 observations. *Astronomy and Astrophysics* 108, 296–305.
- Smith, B. A., Soderblom, L., Batson, R. M., Bridges, P. M., Inge, J. L., Masursky, H., Shoemaker, E., Beebe, R. F., Boyce, J., Briggs, G., Bunker, A., Collins, S. A., Hansen, C., Johnson, T. V., Mitchell, J. L., Terrile, R. J., Cook, A. F., Cuzzi, J. N., Pollack, J. B., Danielson, G. E., Ingersoll, A. P., Davies, M. E., Hunt, G. E., Morrison, D., Owen, T., Sagan, C., Veverka, J., Strom, R., Suomi, V. E., 1982. A new look at the Saturn system—The Voyager 2 images. *Science* 215, 504–537.
- Smith, B. A., Soderblom, L., Beebe, R. F., Boyce, J. M., Briggs, G., Bunker, A., Collins, S. A., Hansen, C., Johnson, T. V., Mitchell, J. L., Terrile, R. J., Carr, M. H., Cook, A. F., Cuzzi, J. N., Pollack, J. B., Danielson, G. E., Ingersoll, A. P., Davies, M. E., Hunt, G. E., Masursky, H., Shoemaker, E. M., Morrison, D., Owen, T., Sagan, C., Veverka, J., Strom, R., Suomi, V. E., 1981. Encounter with Saturn—Voyager 1 imaging science results. *Science* 212, 163–191.
- Zebker, H. A., Marouf, E. A., Tyler, G. L., 1985. Saturn's rings—Particle size distributions for thin layer model. *Icarus* 64, 531–548.
- Zebker, H. A., Tyler, G. L., 1984. Thickness of Saturn's rings inferred from Voyager 1 observations of microwave scatter. *Science* 223, 396–398.